Induced polarization of clay-rich materials. 2. The effect of anisotropy

André Revil, Ahmad Ghorbani, Damien Jougnot, Béatrice Yven, D. Grgic, François Bretaudeau, Jacques Deparis

To cite this version:

André Revil, Ahmad Ghorbani, Damien Jougnot, Béatrice Yven, D. Grgic, et al.. Induced polarization of clay-rich materials. 2. The effect of anisotropy. Geophysics, 2023, 88, pp.1-53. ⟨10.1190/geo2022-0511.1⟩. ⟨hal-04186264⟩

HAL Id: hal-04186264
https://hal.science/hal-04186264v1

Submitted on 26 Aug 2023

Induced polarization of clay-rich materials.
2. The effect of anisotropy

A. Revil (1), A. Ghorbani (2), D. Jougnot (3), B. Yven (4)
D. Grgic (5), F. Bretaudeau (6), and J. Deparis (6)

(1) Univ. Grenoble Alpes, Univ. Savoie Mont-Blanc, CNRS, UMR CNRS 5204,
EDYTEM, 73370 Le Bourget du Lac, France
(2) Naga Geophysics, Technolac, 73370 Le Bourget du Lac, France
(3) Sorbonne Université, CNRS, EPHE, UMR 7619 Metis, 4 Place Jussieu, 75005 Paris, France
(4) ANDRA, Scientific and Technical Division, 1-7 rue Jean Monnet, Parc de la Croix-Blanche, 92298 Châtenay-Malabry cedex, France
(5) Université de Lorraine, GeoRessources, Ecole Nationale Supérieure de Géologie, Nancy, France
(6) BRGM, Orléans, France

Corresponding Author: André Revil (andre.revil@univ-smb.fr)

Emails: ahmad.ghorbani@naga-geophysics.com; damien.jougnot@upmc.fr; beatrice.yven@andra.fr; dragan.grgic@univ-lorraine.fr; j.deparis@brgm.fr; F.Bretaudeau@brgm.fr;

Running title: Induced polarization and anisotropy

Accepted for publication in Geophysics:

Revil, A., Ghorbani, A., Jougnot, D., Yven, B. (2023) Induced polarization of clay-rich materials. Part 2: The effect of anisotropy, Geophysics, 88(4), 1-57, doi:10.1190/geo2022-0510.1.

Abstract. We investigate the anisotropy in the complex conductivity of a clayrock formation through both laboratory and in situ measurements. Laboratory measurements have been conducted on four samples from two cores of the Callovo-Oxfordian formation from the Paris Basin (France). This clay-rock formation is anisotropic with a well-defined bedding plane. Two of the cylindrical core samples are taken in the transverse direction with respect to the bedding plane while two other core samples are taken in the in-plane direction. The complex conductivity spectra are performed in the frequency range 20 mHz to 45 kHz and in a broad pore water saturation range from near saturation to a residual saturation of ~25%. The complex conductivity spectra are fitted with a double Cole Cole model, the low-frequency contribution corresponding to induced polarization effect while the high-frequency contribution is related to the Maxwell-Wagner polarization. The six Cole Cole parameters are investigated as a function of saturation and we evaluate their degree of anisotropy versus the effect of saturation. The low-frequency instantaneous conductivity and normalized chargeability show a consistent degree of anisotropy with an anisotropy ratio equal to 3.8±0.5 for one core sample and 6.5±0.9 for the second core sample. These values represent a substantial level of anisotropy. The low-frequency Cole Cole exponent and relaxation time do not show substantial amount of anisotropy. The monitoring of the evolution of the weight in the controlled humidity chamber seems to indicate that their relative permeabilities do not show a strong anisotropic behavior. Finally, the laboratory data are discussed in the context of field data obtained with an azimuthal array of 12 electrodes.

Introduction

Shale formations including clayrocks, mudstones, claystones, and argillites are low permeability formations that can be used for the geological storage of contaminants including nuclear wastes (Grambow et al., 2014). The development of an operating geological repository for highly radioactive wastes requires the development of research works dedicated to their long-term safety. In this context, the understanding of the properties of the clay formations in their ability to isolate radionuclides (especially most mobile radionuclides such as iodine-129 and chlorine 36) is of paramount importance.

Due to preferential orientation of minerals and finely laminated bedding planes, clay-rich rocks are almost ubiquitously anisotropic in their macroscopic transport properties (Singh and Sircar, 2014). This is especially true for their permeability (e.g., Ashworth and Doster, 2020), their diffusion coefficients (e.g., Zhang et al., 2017) as well as for their mechanical properties (e.g., Cheng, 1997; Coussy, 2003). In the case of the Collavo-Oxfordian clayrocks of the Paris Basin, recent studies have demonstrated a weak anisotropy in their permeability and mechanical properties (Giot et al., 2012, 2014).

Geophysical methods can be used to assess the anisotropy associated with the texture of shales. Various studies have been dedicated to the anisotropy of the seismic velocities of rocks (see for instance Zinszner et al., 2002; Yenugu, 2010; Singh and Sircar, 2014). The impact of the fabric tensor on the electrical conductivity tensor has been investigated by Niu et al. (2017). However, electrical conductivity tomography is difficult to interpret as a stand-alone alone technique because the electrical conductivity of rocks depends on two contributions. These two contributions are the bulk conductivity associated with the saline pore water located in the interconnected pore space and the surface conductivity associated with conduction in the electrical double layer and dependent on their Cation Exchange Capacity, CEC (e.g., Revil et al., 2019, and references therein).

Induced polarization is a geophysical method that extend the electrical conductivity method by looking, in addition to conduction, at the low frequencies (<10 kHz) polarization of porous media. It is currently considered a hot topic in the realms of hydrogeophysics (e.g., Titov et al., 2002; Mwakanyamale et al., 2012; Revil et al., 2012; Kemna et al., 2012) and biogeophysics (e.g., Chen et al., 2009; Abdel Aal et al., 2010, Wainwright et al., 2016). In frequency-domain induced polarization, the conductivity tensor is replaced by a complex-conductivity tensor with components that are frequency-dependent (Revil et al., 2013).

Works dedicated to the study of the anisotropy of clay-rocks in terms of induced polarization parameters are scarce. Zisser and Nover (2009) and Zisser et al. (2010a, b) presented experimental data describing the polarization and anisotropy of tight (low-permeability) sandstones. Revil et al. (2013) developed the first model describing the complex conductivity tensor of transversely anisotropic clay-rocks and mudstones. Additional data were presented by Woodruff et al. (2014, 2015) checking the validity of this model. The anisotropy of the complex conductivity tensor of graphite-bearing rocks was also analyzed recently by Abdulsamad et al. (2020). There is no paper investigating anisotropy of electrical conductivity and normalized chargeability of clay-rocks presenting both laboratory and field data and a theoretical framework to understand these data.

In the present paper, we analyze both laboratory and field low-frequency induced polarization properties of the Callovo-Oxfordian clayrock found in the Paris Basin (France). The anisotropy of this clayrock is analyzed both in the laboratory, at different degree of saturations, and in the in-situ condition of the underground laboratory operated by ANDRA in France (Paris

Basin). Such data are critically needed to evaluate if the use of tomographic codes able to account for anisotropy is needed or not in the context of the storage of radionucleides in the clayrock formations.

Conductivity and normalized chargeability tensors

Isotropic clayrocks

Electrical conductivity and normalized chargeability describe the ability of a rock to transfer electrical charges by conduction and to reversibly store electrical charges, respectively, both under the action of an applied electrical field. Revil (2013) developed a petrophysical model to describe the complex conductivity of clayey materials using a volume-average approach and the dynamic Stern layer concept. We consider below a partially saturated clay-rock at saturation s_w (dimensionless). For an isotropic clayrock, the instantaneous conductivity σ_∞ (in S m^{-1}) of porous materials and the normalized chargeability M_n are given by,

$$\sigma_\infty(s_w) = \frac{1}{F} s_w{}^n \sigma_w + s_w{}^{n-1}\left(\frac{1}{F\phi}\right)\rho_g B \mathrm{CEC}\,, \tag{1}$$

$$M_n(s_w) = s_w{}^{n-1}\left(\frac{1}{F\phi}\right)\rho_g \lambda \mathrm{CEC}\,, \tag{2}$$

where σ_w (in S m^{-1}) denotes the pore water conductivity, ρ_g denotes the mass density of the grains (around 2700 kg m^{-3}), $n \geq 1$ is the saturation exponent (dimensionless, also called the second Archie's exponent), and F (dimensionless) denotes the (intrinsic) formation factor. The formation factor is related to the connected porosity ϕ by Archie's equation $F = \phi^{-m}$ where m (dimensionless) denotes the porosity or first Archie's exponent. The CEC denotes Cation Exchange Capacity of the material (expressed in C kg^{-1} and often expressed in meq/100 g with 1 meq/100 g = 963.20 C kg^{-1}). It can be easily measured through titration experiments (e.g., Aran et al., 2008). A dimensionless number R was introduced by Revil et al. (2017a, b, c) as $\mathrm{R} = \lambda / B$ where λ and B are two apparent mobilities for polarization and conduction. From previous studies (e.g., Ghorbani et al., 2018), we have $B(\mathrm{Na}^+, 25°\mathrm{C}) = 3.1\pm0.3\times10^{-9}$ m^{2}s^{-1}V^{-1} and $\lambda(\mathrm{Na}^+, 25°\mathrm{C}) = 3.0\pm0.7\times10^{-10}$ m^{2}s^{-1}V^{-1}. Both B and λ depends linearly with temperature at a rate of 2% per degree Celcius. Therefore $R \approx 0.10\pm0.02$ (independent of saturation and temperature).

Another very useful relationship can be found between the quadrature conductivity at the geometric mean frequency of two frequencies f_1 and f_2 and the normalized chargeability. The partial normalized chargeability is here defined as the difference between the in-phase conductivity at the frequency $f_2 (> f_1)$ and the in-phase conductivity at the lower frequency f_1. This relationship is given by (Van Voorhis et al., 1973; Revil et al., 2017a)

$$\sigma''\left(\sqrt{f_1 f_2}\right) \approx -\frac{M_n(f_1, f_2)}{\alpha}, \tag{3}$$

$$\alpha \approx \frac{2}{\pi} \ln A, \tag{4}$$

where A corresponds to the number of decades separating f_1 and f_2 (3 decades implies $A = 10^3$ and therefore $\alpha \approx 4.4$). Equations (3) and (4) are independent of both the saturation state of the material and temperature.

Finally, the permeability can be related to a mean pore size Λ and the formation factor F by,

$$k(s_w) \approx k_r(s_w) \frac{\Lambda^2}{8F}, \tag{5}$$

which can be considered as a generalized Kozeny-Carman equation (see Johnson et al. 1989 and Revil et al. 2013). In Equation (5), k_r denotes the relative permeability of the rock and Λ is a hydraulic pore radius. As discussed in Revil et al. (2023), the relative permeability is given by,

$$k_r(s_w) = \left(\frac{s_w - s_w^i}{1 - s_w^i} \right)^{n+2}, \tag{6}$$

where s_w^i (dimensionless) is the irreducible water saturation.

Complex conductivity: anisotropic case

All the anisotropy of the complex conductivity is associated with the anisotropy of the tortuosity tensor. Since porosity is a scalar, this means that the formation factor is a second-order symmetric tensor. The other quantities in the complex conductivity equations do not depend on the anisotropy of the material. A simple generalization of the above expressions to anisotropic media yields the following expression for the instantaneous conductivity tensor:

$$\boldsymbol{\sigma}_\infty = \sigma_{ij}^\infty \mathbf{x}_i \otimes \mathbf{x}_j, \tag{7}$$

$$\sigma_{ij}^\infty \approx F_{ij} \left({s_w}^n \sigma_w + \frac{1}{\phi} {s_w}^{n-1} \rho_g B \mathrm{CEC} \right), \tag{8}$$

where $\mathbf{x}_i$ $(i$ =1, 2, 3) denote the basis vectors of the Cartesian frame of reference $(\mathbf{x}_i \cdot \mathbf{x}_j = \delta_{ij}$ where δ_{ij} denotes the Kronecker delta), $\mathbf{a} \otimes \mathbf{b}$ represents the tensorial product between vectors $\mathbf{a}$ and $\mathbf{b}$. The formation tensor is given by $\mathbf{F} = F_{ij} \mathbf{x}_i \otimes \mathbf{x}_j$, where F_{ij} denotes the components of the (symmetric second-rank) formation factor tensor for the conductivity, that we write as **F**. In the isotropic case $F_{ij} = (1/F)\delta_{ij}$ with F the intrinsic formation factor. This model also assumes that the saturation exponent remains more or less the same in the eigendirections and that the pore sizes are also the same in the eigenvector directions as discussed in the previous paper of this series. We will see later that these assumptions agree well with the experimental data but they should be considered as a simplifications. The tortuosity tensor is simply the formation factor tensors divided by the porosity $\mathbf{T} = \tau_{ij} \mathbf{x}_i \otimes \mathbf{x}_j$ and $\tau_{ij} = F_{ij} / \phi$. The inverse of its component corresponds to the tortuosity of the current flow path in a given direction. Tortuosity is a quantitative measure of the effect of the deviation of the current streamlines from straight (not tortuous) paths in an electrolyte to tortuous paths in a complex porous body.

Neglecting the presence of pyrite, the normalized chargeability tensor can be written as

$$\mathbf{M}_n = M_{ij}^n \mathbf{x}_i \otimes \mathbf{x}_j , \tag{8}$$

$$M_{ij}^n \approx F_{ij} \frac{1}{\phi} s_w^{\,n-1} \rho_g \lambda \mathrm{CEC} . \tag{9}$$

Finally, equation (3) would be preserved for the anistropic case and the relationship between the quadrature conductivity component and the normalized chargeability components would be,

$$\sigma_{ij}''\left(\sqrt{f_1 f_2}\right) \approx -\frac{M_{ij}^n (f_1, f_2)}{\alpha} , \tag{10}$$

where α is the same whatever the directions and given by equation (4).

In the context of the COx formation, we consider that unfractured COx core samples characterized by a bedding plane. The two eigenvectors along the bedding plane correspond to the in-plane direction (index i) while the normal direction is called the transverse direction (index t). If the function EV extracts the eigenvalues of a given tensor, then we have $\mathrm{EV}(\boldsymbol{\sigma}_\infty) = (\sigma_i, \sigma_i, \sigma_t)$ and $\mathrm{EV}(\mathbf{M}_n) = (M_i^n, M_i^n, M_t^n)$. The electrical anisotropy ratio is then defined as $\lambda_e = \sigma_i / \sigma_t = M_i^n / M_t^n$. Consequently, the electrical anisotropy ratio should be the same for the conductivity and the normalized chargeability, i.e., for conduction and polarization processes, which is an important feature of our model. This heuristic prediction can be easily tested with respect to laboratory data.

.

Permeability tensor

Another question is to know if the relative permeability is just a function of saturation and if the effect of the bedding can be neglected. In other word, we write the permeability of the COx as

$$\mathbf{k}(s_w) = k_r(s_w)\mathbf{k}_S = k_r(s_w)k_{ij}\mathbf{x}_i \otimes \mathbf{x}_j \, , \tag{11}$$

where $\mathbf{k}_S$ denotes the permeability tensor at saturation with components k_{ij} and $k_r(s_w)$ is the relative permeability function already defined above (equation 6), and $s_w^i \approx 0.35 \pm 0.05$ denotes the irreducible water saturation for the COx as obtained in the previous paper of this series (Revil et al., 2023).

Assuming that the COx clayrock is characterized by a bedding plane, the eigenvalues of the permeability tensor are $\mathrm{EV}(\mathbf{k}_S) = (k_i, k_i, k_t)$ and the hydraulic anisotropy ratio is defined as $\lambda_h = k_i / k_t$. Then, one of the key questions we want to answer is to know if (and how) the electrical and hydraulic anisotropy ratios are related to each other. If we examine equation 5 and if we consider that the pore sizes are the same in the eigenvectors' directions, then we should expect $\lambda_e \approx \lambda_h$ since $k_{ij} = (\Lambda^2 / 8)F_{ij}$.

Experiments and results

Material and method

The Callovo-Oxfordian (COx) clayrock formation of the Paris Basin is mainly composed by clay minerals (20 to 55%, illite, micas, interstratified illite/smectite, kaoline and chlorite), silica (25 to 35%), calcite (15 to 30%) and secondary minerals (less than 5% of the total) including feldspar, dolomite, hematite and small proportions of pyrite (see Yven et al., 2007, Vinsot et al., 2014, see Paper 1). The Callovo-Oxfordian formation is weakly anisotropic due to a bedding plane (Figure 1) and the presence of small proportion of pyrite (Figure 2).

We consider in the experimental study 2 cores labelled EST59674 and EST59676, respectively. Two samples are drilled in the direction along the bedding and two other samples normal to the bedding plane. So we consider 4 samples in total. The physical properties of these samples are summarized in Table 1. Frequency-domain complex conductivity measurements are performed using the ZELSIP04-V02 impedance meter (Zimmermann et al., 2008) already used in the previous paper of this series. The frequency range investigated is 20 mHz-45 kHz. The measurements are made in a desiccation chamber in which the relative humidity is imposed as described in the previous paper of this series (see Figures 3 and 4). The relative humidity is imposed by using specific salts.

The measured complex conductivity spectra are shown in Figures 5 and 6. We use a Bayesian technique to invert the Cole Cole parameters (Appendix A). The Cole Cole parameters are collected in Tables 2 and 3 for the core sample EST59674 and in Tables 4 and 5 for the core sample EST59676. We observe that both the amplitude of the conductivity and quadrature conductivity decrease with the saturation. For these experiments, we use exactly the same experimental protocol and sample holder as in Revil et al. (2017a) so the details of the experiments will not be repeated here (see also Revil et al., 2023). The complex conductivity spectra are fitted with a double Cole Cole model (see Appendix A). Fits of the complex conductivity spectra are shown in Figures 5 and 6. The double Cole Cole model is clearly able to reproduce the experimental data up to 10 kHz.

The permeability of COx samples to water at full saturation was assessed with the pulse decay method (Brace et al., 1968). This method allows determining both the intrinsic permeability k (m^2) and the specific storage coefficient Ss (m^{-1}) of low permeability materials. Initially, the sample is water-saturated and the fluid pressure inside the sample and the reservoirs is at equilibrium. A rapid increment of the fluid pressure (pulse) is imposed at the upstream reservoir, which create a one-dimensional flow through the saturated porous sample. The fluid pressure obeys a diffusion equation written as

$$\frac{\partial^2 p}{\partial x^2} - \frac{S_S \mu_w}{k \gamma_w} \frac{\partial p}{\partial t} = 0, \qquad (12)$$

where p denotes the fluid pressure in the core sample of length L and for $0 \leq x \leq L$, x (m) is the distance along the sample ($x = 0$: downstream face; $x = L$: upstream face), γ_w denotes the specific weight of the water ($kg.m^{-2}.s^{-2}$), and submitted to specific pressure boundary conditions. Classical solutions have been proposed in the literature assuming uncoupled hydraulic and mechanical behaviors (e.g., Hsieh et al., 1981). In the context of poroelasticity, Homand et al. (2004) proposed an analytical solution for the hydromechanical problem assuming the skeleton of the porous sample is elastic. We implemented this analytical solution in (Wolfram) Mathematica©) and using an inverse method (based on Levenberg-Marquardt algorithm) we fit the pulse test data to obtain the value of the permeability and specific storage. As a side note, Giot et al. (2011) proposed a fully coupled analysis of the pulse test experiment through finite element modelling in 3D. An inversion algorithm for the identification of the poromechanical parameters was also proposed in this paper. By applying this complete solution on the COx claystone/clayrock, Giot et al. (2011)

found that the difference in estimating the intrinsic permeability between the two approaches was less than 15%. Since the 1D analysis gives good results, it was chosen in this study for the sake of simplicity.

Anisotropy of the electrical conductivity

The anisotropy of the instantaneous conductivity is shown in Figure 7. There is a clear anisotropy with a higher electrical conductivity along the bedding plane than with respect to conductivity in the normal direction to the bedding plane. This observation is consistent with our expectation that the bedding plane is more conductive with respect to the transverse direction. The obtained electrical conductivity anisotropy ratios are 4.3±1.0 and 6.0±1.4 for the cores EST59674 and EST59676, respectively. At the opposite, the saturation exponents are nearly the same in the in-plane and transverse directions. We obtain $n = 3.2 \pm 0.3$ validating the assumption made above.

Anisotropy of the normalized chargeability

The anisotropy of the (low-frequency) normalized chargeability is shown in Figure 8. The normalized chargeability displays a clear anisotropy ratio with a higher normalized chargeability in the bedding plane by comparison with the transverse direction. The normalized chargeability anisotropy ratios are 3.1±0.7 and 7.0±1.0 for the cores EST59674 and EST59676, respectively. These values are fairly consistent with the values obtained from the instantaneous conductivity data (4.3±1.0 and 6.0±1.4). The saturation exponent obtained from the normalized chargeability data is also fairly consistent in the in-plane and transverse directions ($n = 3.7 \pm 0.3$). Therefore the value of the saturation exponent and the amplitude of the anistropy ratio are consistent between the electrical conductivity and the normalized chargeability, which observations are in agreement with the predictions of our model.

Anisotropy of the residual saturation

The residual saturation ($s_w^i \approx 0.36 \pm 0.05$) is consistent with that obtained in the previous paper of this series. It is also the same for the instantaneous conductivity and the normalized chargeability and is independent of the direction of the core sample.

Anisotropy of the permeability

The COx clay rock shows anisotropy in its permeability (Giot et al., 2014). Mohajerani et al. (2011) obtained a permeability for the COx of 2.0 $\times 10^{-21}$ m^2 along the bedding plane and 0.6 $\times 10^{-21}$ m^2 in the transverse direction. This yields a hydraulic anisotropic ratio $\lambda_h = 3.3$. Menaceur et al. (2015) and Harrington et al. (2017) found permeabilities in the bedding plane of 9 - 29 $\times 10^{-21}$ m^2 and in the range 4.5 - 7.0 $\times 10^{-21}$ m^2 in the transverse direction. These correspond to anisotropy ratio λ_h in the range 2 to 4. Armand et al. (2017) obtained values of permeability of 3.0 and 6.0 $\times 10^{-20}$ m^2 for perpendicular and parallel directions to the bedding plane, respectively. This yields again in an anisotropy ratio $\lambda_h =$ 2.0. So the anisotropy of the permeability tensor is not very high.

The results of the permeability tests for our core samples are reported in Table 1 and are consistent with the estimates discussed above with estimate of λ_h in the range 1.9 to 3.7. In Figure 9, we plot the hydraulic anisotropy ratio of the two cores as a function of the electrical anisotropy ratio. We also add estimates from the literature. The data are fairly consistent with $\lambda_e \approx \lambda_h$ and therefore also consistent with the findings of Maineult et al. (2018) on pore network simulations.

In other words, the anisotropy of the induced polarization properties and permeabilities are related to an anisotropy of the tortuosity paths rather than a possible anisotropy in the pore sizes.

The previous argument can be checked independently. The low-frequency Cole Cole exponent described the broadness of the relaxation times for induced polarization. These relation times can be related to the pore sizes as discussed in Tartrat et al. (2019). Figure 10 shows that the (low-frequency) Cole Cole exponent c_1 is independent of the direction indicating that the broadness of the relaxation times is the same in the bedding plane and normal to the bedding plane (Figure 11).

The next point to check is the validity of equation (11). In other words, can be separate the permeability tensor at a given saturation as the product of a scalar function depending only on the saturation and a permeability tensor at saturation. In order to reply to this question, we closely look at the desaturation curves shown in Figure 2. In Figures 12 and 13, we look at the relaxation of the mass of the core samples when the relative humidity is changed in the humidity chamber. We observe that the relaxation times are nearly independent of the direction, which may indicate that the relative permeability function can be considered as a scalar in first approximation. This is consistent with the fact that we have already demonstrated that n and s_w^i are independent of the direction with respect to the bedding plane.

Field test

An experiment was carried out at the ANDRA Underground Research Laboratory (URL) located near Bure in France (see Figure 14a., Armand et al., 2014). This URL is dedicated to digging activities, technological demonstrations and scientific experiments for the design of the geological disposal facility for radioactive waste. is The experimental galleries are located in the COx formation at a depth of ~500m. We performed azimuthal measurements to characterize the anisotropy of both the conductivity and normalized chargeability in the COx formation at Bure inside the galleries of the URL. Four boreholes with a length of 22 m were drilling from the main gallery. Figure 14b. shows a sketch of the position of each borehole from the main gallery.

For each borehole (labeled AHA1612 to AHA1615), two rings of electrodes allowing to measure the anisotropy of the complex resistivity are installed at 17.9 and 18.2 meters from the gallery wall. Each device therefore contains two ring composed by twelves stainless steel electrodes (Figure 14c). The 10 mm-diameter electrodes are placed in a plastic cylinder of external diameter 121 mm and spaced 30 degrees apart (Figure 14d). Each electrode ring is wired with a multi-pair shielded cable. The purpose of this connection is to isolate each electrode by the shielding of the pair and thus and therefore limit the effects of induction from one conductor to the other. Resin coats all the cable and electrode connections. The device is finally placed inside the borehole as close as possible to the inner walls (131 mm diameter), leaving a spacing of approximately 5 mm. Indeed, the positioning of the rings is ensured by the use of benders. To ensure electrical contact with the electrode and COx formation, the probes were sealed after installation with a conductive bentonite cement grout.

The measurements were carried out using the SYSCAL Pro Impedance meter using a dipole–dipole array. The SYSCAL PRO include the current injection system, the potential difference measurement system, as well as a multiplexer allowing the acquisition of injection/measurement sequences programmed beforehand. The system also includes a stabilized and decoupled power supply, as well as a computer allowing the repetition over time of the measurement sequences, the remote control of the system and the storage of data.

In this field experiment, the contact resistances were comprised between 4 to 10 kΩ and the injected current varies from 200 to 500 mA. The measurements are presented using radial figures. This is a representation of the conductivity and normalized chargeability measurements as a function of the orientation of the center of the quadrupole on the measurement ring.

For each ring, twelves measurement were carried out. Measurement 1 corresponds to the measurement between electrodes 1-2-3-4 (45° azimuthal correspondence). Here the injection of the current is carried out between electrodes 1 and 2 and the potential is measured between the electrodes 3 and 4. Measurement 2 corresponds to the measurement between electrodes 2-3-4-5 (75° azimuthal correspondence) and so on until last measurement between electrodes 12-1-2-3 (15° azimuthal correspondence). Figure 15a., b., c. show the resistivity diagrams obtained on one ring for this configuration acquired respectively for the rings 1, 4, 5 inside borehole 1612, 1613 and 1614. That said, since the rings behave differently in different boreholes, this indicates that the effect of the heterogeneity associated with damage around the wells is important. As a first approximation, we see that the diagrams show a marked anisotropic behavior with apparent conductivities on the order of 0.14 S m^{-1} in the horizontal direction and around 0.08 S m^{-1} in the vertical direction as determined from the apparent resistivities. These values are fairly consistent with the conductivity data obtained in the laboratory experiments presented above (see also Figure 7). The different may be explained through the existence of cracks associated with damage of the COx formation around the boreholes.

Figures 15d.e.f show the chargeability diagrams obtained on one ring for the same configuration as the electrical measurements and acquired respectively for the ring 1, 4, 5 inside borehole 1612, 1613 and 1614, respectively. The chargeability data is noisy because the EM noise is high in the underground laboratory. As electrical resistivity, the anisotropy highlight the effect of the heterogeneity associated with damage around the borehole. The shape of chargeability diagram is quite similar than the resistivity diagram. The diagram highlights a marked anisotropic behavior with apparent chargeability on the order of 15 mV/V in the horizontal direction and around 25 mV/V in the vertical direction. Figure 16a shows the mean chargeability of the 8 rings. This is expected since chargeability is a ratio between the normalized chargeability and the conductivity, which share the same eigenvectors and the same ratio of the eigenvalues. This is consistent with the laboratory data shown in Figure 16b.

Conclusion

We have measured the complex conductivity spectra of two core samples from the Callovo-Oxfordian (COx) formation of the Paris Basin in the frequency range 20 mHz to 45 kHz. The spectra were fitted with a double Cole Cole model with one contribution associated with the polarization of the electrical double layer and a second polarization associated with the Maxwell-Wagner (interfacial) polarization. The measured were both performed in the direction and normal to the bedding plane of the core samples. The two core samples exhibit a clear anisotropy in their instantaneous conductivity and normalized chargeability. The instantaneous conductivity and normalized chargeability of the first core sample exhibit an anisotropy ratio of 3.8±0.5 while the second core sample is characterized by an anisotropy ratio of 6.5±0.9 in the saturation range 0.36 to 0.97. The Cole Cole exponent and the low-frequency Cole Cole relaxation times are independent of the direction. The anisotropy ratio obtained from the electrical conductivity and normalized chargeability can be related to the anisotropy ratio of the permeability. This indicates in turn that the pore sizes do no depend on the direction in the COx formation. The saturation exponent and the residual water saturation are found to be independent of the direction. This is consistent with the observation that the relative permeability is also independent of the direction with respect to the bedding plane. Finally, a field experiment is carried out to check the anisotropy of the conductivity and normalized chargeability directly in the COx formation at a depth of 500 m.

Acknowledgments. We thank E. Zimmermann for his impedance meter. We thank the French National Radioactive Waste Management Agency (ANDRA) for its financial support and for providing the core samples used in this study. We thank Timothé Tartrat for his help with the measurements. A. Revil thanks the French National Research Agency (ANR) through the HYDROGEODAM project under grant no. ANR-17-CE06–0016, for funding his contribution. We thank the Editor, Vincenzo Lapenna and an anonymous referee for their constructive review of our manuscript.

References

Abdel Aal, G. Z., E. A. Atekwana, S. Rossbach, and D. D. Werkema (2010), Sensitivity of geoelectrical measurements to the presence of bacteria in porous media: J. Geophys. Res., 115, G03017, doi:10.1029/2009JG001279.

Abdulsamad F., A. Revil, A. Ghorbani, V. Toy, M. Kirilova, A. Coperey, P.A. Duvillard, G. Ménard, and L. Ravanel, 2020, Complex conductivity of graphitic schists and sandstones: Journal of Geophysical Research, **124**, 8223–8249. doi: 10.1029/2019JB017628.

Adams; A.L., T.J. Nordquist, J.T; Germaine, and P.B. Flemings 2016, Permeability anisotropy and resistivity anisotropy of mechanically compressed mudrocks: Canadian Geotechnical Journal. 41 pp. doi: 10.1139/cgj-2015-0596.

Aran, D., A., Maul, and J. F., Masfaraud, 2008. A spectrophotometric measurement of soil cation exchange capacity based on cobaltihexamine chloride absorbance: Comptes Rendus Geoscience, **340**(12), 865–871. doi:10.1016/j.crte.2008.07.015.

Armand G., Leveau F., Nussbaum C. , de La Vaissiere R. , Noiret A. , Jaeggi D. , Landrein P. , Righini C. , 2014, Geometry and properties of the excavation-induced fractures at the Meuse/Haute-Marne URL Drifts: Rock Mechanics and Rock Engineering, **47**, 1, 21–41.

Armand, G., F., Bumbieler, N., Conil, R., de la Vaissière, J. M., Bosgiraud, and M. N. Vu, 2017, Main outcomes from in situ thermo-hydro-mechanical experiments program to demonstrate feasibility of radioactive high-level waste disposal in the Callovo-Oxfordian claystone: Journal of Rock Mechanics and Geotechnical Engineering, **9**(3), 415–427

Ashworth, M., Doster, F., 2020. Anisotropic dual-continuum representations for multiscale poroelastic materials: Development and numerical modelling: International Journal for

Numerical and Analytical Methods in Geomechanics, **44**, 2304–2328. doi: 10.1002/nag.3140, doi:10.1002/nag.3140.

Bretaudeau F., J., Deparis, B.Yven, 2021. Evaluation de la sensibilité des méthodes géophysiques pour la caractérisation et le suivi spatio-temporel de la zone endommagée autour des alvéoles HA: Rapport final. Analyse des données et interprétation. BRGM/RP**-71331** –FR

Chen, J., S. S. Hubbard, K. H. Williams, S. Pride, L. Li, and L. Slater, 2009. A state-space Bayesian framework for estimating biogeochemical transformations using time-lapse geophysical data: Water Resour. Res., 45, W08420, doi:10.1029/2008WR007698.

Cheng, A.H.D., 1997. Material coefficients of anisotropic poroelasticity: International Journal of Rock Mechanics and Mining Sciences 34, 199–205. doi: 10.1016/S0148-9062(96)00055-1.

Coussy, O., 2003. Poromechanics. John Wiley & Sons, Ltd, Chichester, UK. doi:10.1002/0470092718.

Gernez, S., A. Bouchedda, E. Gloaguen and D. Paradis, 2019. Comparison between hydraulic conductivity anisotropy and electrical resistivity anisotropy from tomography inverse modeling: Front. Environ. Sci., **7**(67). doi: 10.3389/fenvs.2019.000.

Giot R., A. Giraud, C. Auvray, F. Homand, and T.Guillon, 2011. Fully coupled prormechanical back analysis of the pulse test by inverse method. Int J Numer Anal Meth Geomech 35(3), 329–359.

Giot R., A. Giraud, T. Guillon, and C. Auvray, 2012. Three-dimensional poromechanical back analysis of the pulse test accounting for transverse isotropy: Acta Geotechnica, **3**, doi 10.1007/s11440-012-0158-7.

Giot, R., Giraud, A., & Auvray, C., 2014. Assessing the permeability in anisotropic and weakly permeable porous rocks using radial pulse tests: Oil & Gas Science and Technology–Revue d'IFP Energies nouvelles, **69**(7), 1171-1189.

Grambow B., Landesman, C., and Ribet S., 2014. Nuclear waste disposal: I. Laboratory simulation of repository properties: Applied Geochemistry, **49**, 237-246. doi: 10.1016/j.apgeochem.2014.05.017.

Harrington, J. F., R. J., Cuss, and J., Talandier, 2017, Gas transport properties through intact and fractured Callovo-Oxfordian mudstones: Geological Society, London, Special Publications, **454**(1), 131–154.

Maineult, A., Jougnot, D., and Revil, A. 2018, Variations of petrophysical properties and spectral induced polarization in response to drainage and imbibition: a study on a correlated random tube network: Geophysical Journal International, **212**(2), 1398-1411.

Menaceur, H., P., Delage, A.-M., Tang, and N. Conil, 2015, The thermo-mechanical behaviour of the Callovo-Oxfordian claystone: International Journal of Rock Mechanics and Mining Sciences **78**, 290–303.

Mohajerani, M., P., Delage, M., Monfared, A.-M., Tang, J., Sulem, and B., Gatmiri, 2011, Oedometric compression and swelling behaviour of the Callovo-Oxfordian argillite: International Journal of Rock Mechanics and Mining Sciences, **48**(4), 606–615

Mosegaard, K., and A. Tarantola, 1995, Monte Carlo sampling of solutions to inverse problems: Journal of Geophysical Research, **100**, 12431–12447, doi: 10.1029/94JB03097.

Mwakanyamale, K., L. Slater, A. Binley, and D. Ntarlagiannis, 2012. Lithologic imaging using induced polarization: Lessons learned from the Hanford 300 area: Geophysics, **77**, 397–409.

Niu, Q., A. Revil, Z. Li, and Y.-H. Wang, 2017. Relationship between electrical conductivity anisotropy and fabric anisotropy in granular materials during drained triaxial compressive tests: a numerical approach: Geophysical Journal International, **210**, 1, 1-17, doi: 10.1093/gji/ggx140.

Revil A., W.F. Woodruff, C. Torres-Verdín, and M. Prasad, 2013. Complex conductivity tensor of hydrocarbon-bearing shales and mudrocks: Geophysics, **78**, no. 6, D403-D418, doi: 10.1190/GEO2013-0100.1.

Revil A., Y. Qi, A. Ghorbani, A. Coperey, A. Soueid Ahmed, A. Finizola, and T. Ricci, 2019. Induced polarization of volcanic rocks. 3. Imaging clay cap properties in geothermal fields: Geophysical Journal International, **218**, no. 2, 1398–1427, https://doi.org/10.1093/gji/ggz207.

Revil, A., A. Ghorbani, D. Jougnot, and B. Yven, 2023. Induced polarization of clay-rich materials — Part 1: The effect of desiccation: Geophysics, **88**, no. 4, https://doi.org/10.1190/GEO2022-0510.1.

Singh A., and A. Sircar 2014. Sources and measurement of velocity anisotropy of Cambay shale, Cambay Basin, India: IJLTEMAS, III(V), 169-172, ISSN 2278 – 2540.

Tartrat Y. T., A. Revil, F. Abdulsamad, A. Ghorbani, D. Jougnot, A. Coperey, B. Yven, and R. de la Vaissière, 2019. Induced polarization response of porous media with metallic particles – Part 10. Influence of desiccation: Geophysics, **84**(5), A43-W32. Doi: 10.1190/geo2019-0048.1.

Titov, K., V. Komarov, V. Tarasov, and A. Levitski, 2002. Theoretical and experimental study of time domain induced polarization in water saturated sands, J. Appl. Geophys., **50**, 417–433, doi: 10.1016/S0926-9851(02)00168-4.

Oxidation front and oxygen transfer in the fractured zone surrounding the Meuse/Haute-Marne URL drifts in the Callovian–Oxfordian argillaceous rock**:** Geological Society, London, Special Publications, 400, 207-220. Doi; 10.1144/SP400.37**.**

Wainwright, H. M., A. Flores Orozco, M. Bücker, B. Dafflon, J. Chen,S. S. Hubbard, and K. H. Williams, 2016, Hierarchical Bayesian method for mapping biogeochemical hot spots using induced polarization imaging: Water Resour. Res., **52**, 533–551, doi:10.1002/2015WR017763.

Woodruff W. F., A. Revil, and C. Torres-Verdín, 2014. Laboratory determination of the complex conductivity tensor of unconventional anisotropic shales: Geophysics, **79**(5), E183–E200, doi: 10.1190/GEO2013-0367.1.

Woodruff W. F., A. Revil, M. Prasad, and C. Torres-Verdín, 2015. Measurements of elastic and electrical properties of an unconventional organic shale under differential loading: Geophysics, **80**(4), D363-D383, doi: 10.1190/GEO2014-0535.1.

Yenugu, M. M., 2010. Ultrasonic measurements of Anisotropy of Shales, PhD thesis, School of Geology and Geophysics, University of Oklahoma, USA, 15 December, 2010.

Yven, B., S., Sammartino, Y., Géraud, H., Homand, and F., Villiéras,, 2007. Mineralogy, texture and porosity of Callovo-Oxfordian argillites of the Meuse/Haute-Marne region (Eastern Paris Basin): Mémoire de la Société Géologie de France, **178**, 73–90.

Zhang,Y. P., Mostaghimi, A., Fogden, A., Arena, A., Sheppard, J.P., Middleton, and R.T., Armstrong, 2017, Determination of local diffusion coefficients and their directional anisotropy in shale, and relations to local mineralogy and organic matter content, from Dynamic Micro-CT imaging and microscopy, Proceedings of the 5th Unconventional Resources Technology Conference, URTeC: 2695407. doi: 10.15530/urtec-2017-2695407.

Zimmermann, E., A., Kemna, J., Berwix, W., Glaas, H. M., Münch, and J. A. Huisman,, 2008, A high-accuracy impedance spectrometer for measuring sediments with low polarizability: Measurement Science and Technology, **19**(10), 105603. Doi: 10.1088/0957-0233/19/10/105603.

Zinszner, B., P., Meynier, J., Cabrera, and P., Volant, 2002, Ultrasonic, sonic and seismic waves velocity in shale from Tournemire tunnel. Impact of anisotropy and natural fractures: Oil & Gas Science and Technology, **57**(4), 341-353.

Zisser, N., and G. Nover, 2009, Anisotropy of permeability and complex resistivity of tight sandstones subjected to hydrostatic pressure: Journal of Applied Geophysics, **68**, 356–370.

Zisser, N., A. Kemna, and G. Nover, 2010a, Dependence of spectral induced polarization response of sandstone on temperature and its relevance to permeability estimation: Journal of Geophysical Research, **115**, B09214, doi:10.1029/2010JB007526.

Zisser N., A. Kemna A. and G. Nover, 2010b, Relationship between low-frequency electrical properties and hydraulic permeability of low-permeability sandstones: Geophysics, **75**, E131-E141. doi: 10.1190/1.3413260.

Appendix A. Double Cole Cole parametric model

In each eigenvector direction, the complex conductivity data is fitted with a double Cole Cole parametric model for which the low frequency polarization is labelled 1 while the higher frequency polarization is labeled 2:

$$\sigma^{*} = \sigma_{\infty}\left(1 - \frac{M_1}{1+(i\omega\tau_1)^{c_1}} - \frac{M_2}{1+(i\omega\tau_2)^{c_2}}\right). \tag{A1}$$

where M_1 and M_2 (dimensionless)denote the chargeabilities, c_1 and c_2 (dimensionless) are the two Cole-Cole exponents, and τ_1 and τ_2 are the (relaxation) time constants (in s). We consider that the low-frequency contribution is the one associated with induced polarization.

We use a Monte Carlo Markov Chain (MCMC) sampling algorithm and a Bayesian approach (Mosegaard and Tarantola, 1995) to invert the in-phase and quadrature conductivity spectra shown in Figures 5 and 6. The model vector contained a form of the Cole Cole parameters is $\mathbf{m} = [\log(\sigma_0); M_1; c_1; \log(\tau_1); M_2; c_2; \log(\tau_2)]$. Then, the algorithm combines this information with the observed data vector and with the information provided by the double Cole-Cole model to obtain optimal realization of the model vectors. The Root Mean Square (RMS) error is given on the MCMC chain has converged as:

$$\mathrm{RMS}^2 = \frac{1}{N}\sum_{i=1}^{N}\left(\frac{g^i(\mathbf{m}) - d^i_{obs}}{d^i_{obs}}\right)^2 , \tag{A2}$$

where $g(\mathbf{m})$ denotes the predicted in-phase or quadrature conductivity spectra and N denotes the number of data used in the fitting process. The fit are shown in Figures 5 and 6.

Tables

Table 1. Characteristics of four core samples investigated in the present study. CEC denotes the Cation Exchange Capacity, which is expressed here in meq/100 g (= 963.20 C kg^{-1}). The porosity was computed by measuring the weight of the saturated and dry core samples and their volume. The permeability appears also anisotropic with a permeability anisotropic ratio λ_k = 1.06 for the core EST59676 (electrical anisotropy ratio 6.5±0.9) and λ_k = 1.9 for core EST59674 (electrical anisotropy ratio 2.0±0.2). φ_m denotes the volume fraction of pyrite from X-ray tomography. The grain density of the core samples is 2710 kg m^{-3}.

Sample	Direction	Porosity ϕ (-)	CEC (meq/100 g)	BET (m^2/g)	k (m^2)	φ_m(-)
EST59676 42	In-plane	0.122	16.83	29.95	1.31×10^{-20}	0.25
EST59676 41	Transverse	0.126	16.83	29.95	1.24×10^{-20}	0.38
EST59674 42	In-Plane	0.130	16.97	30.46	2.93×10^{-20}	0.29
EST59674 41	Transverse	0.148	16.97	30.46	1.45×10^{-20}	0.22

Table 2. Inversion of the Cole Cole parameters for the core sample EST59674-41 (tranverse direction). Index 1 is used for the low frequency contribution which is associated with the induced polarization contribution.

s_w	τ_1(s)	τ_2(s)	c_1 (-)	c_2 (-)	M_1 (-)	M_2 (-)	σ_∞ (S/m)	RMS (%)
0.965	0.00859	1.52e-05	0.550	0.541	0.0459	0.0647	0.0321	0.246
0.965	0.00670	4.34e-06	0.461	0.456	0.0260	0.0859	0.0282	0.227
0.781	0.0127	8.48e-07	0.465	0.548	0.0293	0.214	0.0159	0.574
0.781	0.0135	1.43e-06	0.501	0.567	0.0145	0.267	0.0167	0.212
0.768	0.00595	1.79e-06	0.450	0.559	0.0200	0.186	0.0148	0.152
0.723	0.00611	4.72e-06	0.462	0.607	0.0252	0.129	0.0120	0.276
0.691	0.00960	2.75e-06	0.453	0.576	0.0232	0.175	0.0111	0.350
0.691	0.0115	1.66e-06	0.483	0.540	0.0207	0.204	0.0115	0.333
0.675	0.0140	2.78e-06	0.501	0.547	0.0204	0.184	0.0102	0.271
0.675	0.0148	5.31e-06	0.518	0.545	0.0189	0.142	0.0107	0.173
0.666	0.00564	4.52e-06	0.424	0.599	0.0257	0.160	0.00887	0.112
0.661	0.00422	4.00e-06	0.422	0.603	0.0271	0.170	0.00858	0.111
0.654	0.00279	1.44e-06	0.399	0.533	0.0228	0.221	0.00926	0.102
0.642	0.00585	4.07e-06	0.458	0.551	0.0211	0.160	0.00852	0.143
0.642	0.00186	3.78e-06	0.405	0.588	0.0273	0.156	0.00904	0.126
0.630	0.00150	3.70e-06	0.381	0.595	0.0287	0.160	0.00866	0.101
0.615	0.00221	1.76e-06	0.388	0.560	0.0242	0.212	0.00906	0.139
0.604	0.000844	2.08e-06	0.361	0.582	0.0310	0.185	0.00902	0.0885
0.592	0.000937	1.11e-06	0.385	0.559	0.0262	0.221	0.0111	0.165
0.582	0.00167	1.58e-06	0.404	0.562	0.0235	0.214	0.00909	0.0931
0.541	0.00205	3.14e-06	0.415	0.600	0.0296	0.188	0.00730	0.102
0.489	0.00234	3.62e-06	0.432	0.623	0.0345	0.214	0.00570	0.154
0.461	0.00228	9.32e-06	0.471	0.708	0.0406	0.169	0.00444	0.199
0.394	0.00303	4.16e-06	0.459	0.620	0.0343	0.310	0.00281	0.171
0.394	0.00294	3.94e-06	0.445	0.626	0.0353	0.319	0.00282	0.173
0.358	0.00123	3.64e-06	0.430	0.655	0.0519	0.294	0.00292	0.0944
0.329	0.00148	5.10e-06	0.430	0.687	0.0596	0.293	0.00221	0.132
0.314	0.00204	2.90e-06	0.432	0.655	0.0525	0.382	0.00214	0.150
0.296	0.00252	5.20e-06	0.428	0.680	0.0589	0.353	0.00165	0.157
0.286	0.00135	5.78e-06	0.401	0.726	0.0748	0.346	0.00149	0.182
0.274	0.00107	4.33e-06	0.385	0.729	0.0757	0.406	0.00141	0.172
0.266	0.000781	5.16e-06	0.365	0.755	0.0841	0.406	0.00122	0.241
0.257	0.00216	5.93e-06	0.408	0.710	0.0699	0.433	0.000975	0.262
0.253	0.00194	5.98e-06	0.406	0.738	0.0727	0.471	0.000816	0.313
0.249	0.000848	9.22e-06	0.383	0.817	0.101	0.407	0.000717	0.274
0.246	0.000719	7.96e-06	0.352	0.784	0.0964	0.446	0.000705	0.243
0.242	0.000469	9.38e-06	0.332	0.802	0.111	0.413	0.000674	0.326
0.239	0.000738	7.23e-06	0.356	0.751	0.0929	0.466	0.000674	0.259
0.235	0.000855	8.14e-06	0.355	0.787	0.0909	0.467	0.000655	0.277
0.230	0.000887	7.95e-06	0.350	0.768	0.0876	0.489	0.000620	0.292
0.230	0.000442	1.15e-05	0.383	0.825	0.106	0.345	0.000752	0.255

Table 3. Inversion of the Cole Cole parameters for the core sample EST59674-42 (in-plane direction along the bedding plane). Index 1 is used for the low frequency contribution which is associated with the induced polarization contribution.

s_w	τ_1(s)	τ_2(s)	c_1 (-)	c_2 (-)	M_1 (-)	M_2 (-)	σ_∞ (S/m)	RMS (%)
0.967	0.0214	4.43e-05	0.688	0.471	0.0237	0.0493	0.0975	0.624
0.967	0.00990	1.22e-05	0.535	0.533	0.0206	0.0510	0.0971	0.194
0.780	0.0360	6.18e-06	0.577	0.445	0.0150	0.0956	0.0654	0.276
0.763	0.0169	3.06e-06	0.477	0.454	0.0138	0.110	0.0666	0.105
0.722	0.0414	8.35e-06	0.481	0.511	0.0173	0.0893	0.0606	0.188
0.694	0.0317	4.70e-06	0.524	0.446	0.0139	0.113	0.0565	0.296
0.678	0.0429	6.88e-06	0.466	0.497	0.0241	0.102	0.0532	0.237
0.678	0.0201	7.06e-06	0.490	0.483	0.0121	0.101	0.0501	0.177
0.669	0.0137	9.93e-06	0.444	0.527	0.0172	0.101	0.0402	0.162
0.664	0.0229	7.14e-06	0.517	0.470	0.0122	0.122	0.0385	0.252
0.664	0.00598	9.36e-06	0.439	0.549	0.0196	0.0964	0.0392	0.156
0.657	0.00828	1.06e-05	0.459	0.533	0.0187	0.0976	0.0364	0.126
0.645	0.00920	4.06e-06	0.465	0.468	0.0167	0.127	0.0383	0.104
0.645	0.00354	2.47e-06	0.386	0.454	0.0152	0.140	0.0459	0.0818
0.632	0.00985	5.34e-06	0.458	0.478	0.0119	0.120	0.0443	0.173
0.617	0.00141	3.57e-06	0.357	0.529	0.0259	0.113	0.0472	0.100
0.617	0.00583	1.43e-05	0.469	0.583	0.0204	0.0815	0.0384	0.238
0.599	0.00533	5.17e-06	0.427	0.496	0.0177	0.112	0.0400	0.107
0.587	0.00221	1.48e-06	0.347	0.428	0.0182	0.155	0.0458	0.188
0.587	0.000530	8.06e-06	0.353	0.584	0.0284	0.0808	0.0545	0.130
0.577	0.00828	2.16e-06	0.421	0.429	0.0105	0.156	0.0488	0.0897
0.541	0.00423	7.32e-06	0.421	0.539	0.0217	0.112	0.0369	0.0855
0.495	0.00966	8.22e-06	0.492	0.516	0.0188	0.132	0.0305	0.170
0.483	0.00948	1.48e-05	0.508	0.567	0.0212	0.118	0.0269	0.271
0.468	0.0248	1.25e-05	0.539	0.510	0.0149	0.137	0.0266	0.258
0.451	0.00918	9.74e-06	0.520	0.504	0.0177	0.148	0.0247	0.188
0.441	0.00248	8.05e-06	0.438	0.553	0.0277	0.144	0.0232	0.125
0.429	0.00453	6.05e-06	0.425	0.493	0.0210	0.169	0.0218	0.144
0.394	0.00679	1.12e-05	0.541	0.529	0.0196	0.169	0.0139	0.237
0.364	0.00608	1.40e-05	0.542	0.560	0.0245	0.166	0.0109	0.218
0.340	0.00519	1.56e-05	0.533	0.591	0.0308	0.165	0.00919	0.250
0.326	0.00655	1.39e-05	0.544	0.549	0.0268	0.185	0.00878	0.264
0.310	0.00657	1.83e-05	0.557	0.601	0.0323	0.174	0.00760	0.397
0.300	0.0173	1.53e-05	0.625	0.511	0.0191	0.210	0.00741	0.352
0.288	0.0140	1.16e-05	0.641	0.510	0.0199	0.234	0.00691	0.430
0.281	0.0132	1.17e-05	0.619	0.497	0.0199	0.242	0.00618	0.402
0.272	0.00924	1.28e-05	0.595	0.538	0.0296	0.240	0.00501	0.491
0.267	0.00863	1.89e-05	0.591	0.574	0.0359	0.227	0.00397	0.450
0.263	0.00531	1.47e-05	0.553	0.592	0.0446	0.233	0.00377	0.439
0.259	0.00881	1.28e-05	0.614	0.535	0.0328	0.262	0.00355	0.509
0.255	0.0104	1.57e-05	0.630	0.528	0.0306	0.262	0.00343	0.440
0.252	0.0113	1.40e-05	0.646	0.547	0.0311	0.275	0.00326	0.465
0.247	0.00863	1.78e-05	0.626	0.577	0.0364	0.252	0.00315	0.467
0.244	0.0132	1.65e-05	0.533	0.705	0.0288	0.275	0.00285	0.475
0.241	0.00941	2.01e-05	0.686	0.569	0.0362	0.255	0.00274	0.593

Table 4. Inversion of the Cole Cole parameters for the core sample EST59676-41 (transverse direction). Index 1 is used for the low frequency contribution which is associated with the induced polarization contribution.

s_w	τ_1(s)	τ_2(s)	c_1 (-)	c_2 (-)	M_1 (-)	M_2 (-)	σ_∞ (S/m)	RMS (%)
0.973	0.00818	2.97e-06	0.745	0.402	0.0181	0.0914	0.0291	0.661
0.973	0.0109	1.02e-06	0.512	0.501	0.0177	0.102	0.0272	0.465
0.810	0.0625	2.32e-06	0.336	0.540	0.0328	0.0984	0.0181	0.147
0.799	0.0128	5.66e-06	0.689	0.531	0.0108	0.0877	0.0210	0.264
0.755	0.0206	4.36e-06	0.793	0.466	0.0113	0.107	0.0198	0.341
0.724	0.0528	4.24e-06	0.415	0.571	0.0346	0.102	0.0188	0.273
0.709	0.0153	3.76e-06	0.528	0.518	0.0132	0.111	0.0165	0.206
0.699	0.0154	3.55e-06	0.619	0.667	0.0199	0.219	0.00337	0.301
0.693	0.0154	2.85e-06	0.604	0.654	0.0199	0.240	0.00329	0.351
0.693	0.00417	9.50e-06	0.586	0.660	0.0221	0.103	0.00335	0.246
0.686	0.00870	1.07e-05	0.673	0.594	0.0185	0.0991	0.00323	0.280
0.672	0.00840	1.01e-05	0.621	0.660	0.0240	0.0982	0.00317	0.290
0.672	0.00164	1.32e-05	0.483	0.907	0.0240	0.110	0.00232	0.284
0.659	0.00254	1.05e-05	0.501	0.867	0.0208	0.116	0.00186	0.279
0.643	0.00609	3.75e-06	0.652	0.595	0.0163	0.154	0.00451	0.213
0.632	0.00675	1.02e-05	0.645	0.694	0.0197	0.108	0.00387	0.313
0.619	0.00448	6.03e-06	0.514	0.757	0.0268	0.136	0.00403	0.449
0.619	0.00269	1.78e-05	0.571	0.858	0.0275	0.0682	0.00543	0.347
0.608	0.00256	1.03e-05	0.587	0.797	0.0269	0.100	0.00459	0.155
0.563	0.00203	1.27e-05	0.472	0.895	0.0422	0.0758	0.00352	0.814
0.505	0.00249	8.52e-06	0.383	0.877	0.0571	0.107	0.00255	0.748
0.492	0.00512	6.06e-06	0.376	0.841	0.0592	0.144	0.00215	0.677
0.405	0.00148	7.37e-06	0.536	0.721	0.0332	0.219	0.00200	0.168
0.365	0.00510	6.20e-06	0.603	0.645	0.0243	0.223	0.00161	0.283
0.334	0.00808	7.47e-06	0.603	0.696	0.0273	0.250	0.00110	0.397
0.317	0.0152	1.48e-05	0.592	0.665	0.0284	0.192	0.000763	0.350
0.299	0.0130	1.03e-05	0.520	0.769	0.0342	0.281	0.000597	0.511
0.288	0.0270	4.62e-06	0.545	0.680	0.0265	0.364	0.000537	0.463
0.276	0.0116	1.24e-05	0.424	0.809	0.0405	0.321	0.000395	0.558
0.268	0.0287	1.11e-05	0.421	0.865	0.0299	0.451	0.000271	0.966
0.255	0.0177	8.98e-06	0.411	0.862	0.0332	0.521	0.000224	0.842
0.251	0.0476	1.23e-05	0.461	0.893	0.0290	0.499	0.000187	0.834
0.248	0.0579	6.31e-06	0.477	0.848	0.0182	0.671	0.000255	0.908
0.244	0.0387	1.37e-05	0.423	0.936	0.0285	0.548	0.000182	0.789
0.242	0.0319	8.13e-06	0.397	0.911	0.0250	0.634	0.000202	0.887
0.238	0.129	1.19e-05	0.565	0.867	0.0181	0.604	0.000176	1.37
0.235	0.0843	1.47e-05	0.513	0.994	0.0222	0.580	0.000148	1.49
0.233	0.0683	9.45e-06	0.465	0.844	0.0189	0.659	0.000178	1.55

Table 5. Inversion of the Cole Cole parameters for the core sample EST59676-42 (in-plane direction). Index 1 is used for the low frequency contribution which is associated with the induced polarization contribution.

s_w	τ_1(s)	τ_2(s)	c_1 (-)	c_2 (-)	M_1 (-)	M_2 (-)	σ_∞ (S/m)	RMS (%)
0.965	0.00716	1.42e-06	0.507	0.383	0.0366	0.0998	0.0987	0.268
0.807	0.0370	4.70e-07	0.530	0.361	0.0291	0.184	0.0587	0.272
0.789	0.0122	1.19e-06	0.425	0.448	0.0302	0.147	0.0652	0.166
0.752	0.0211	1.13e-06	0.467	0.440	0.0336	0.162	0.0615	0.214
0.723	0.0450	5.91e-07	0.435	0.440	0.0414	0.200	0.0582	0.239
0.708	0.0713	9.25e-07	0.489	0.436	0.0518	0.192	0.0529	0.163
0.708	0.0147	8.52e-07	0.415	0.413	0.0202	0.183	0.0513	0.117
0.694	0.0151	6.74e-07	0.436	0.414	0.0230	0.204	0.0441	0.137
0.679	0.0164	2.26e-06	0.427	0.473	0.0275	0.161	0.0385	0.157
0.679	0.0212	7.29e-07	0.441	0.396	0.0163	0.197	0.0482	0.110
0.668	0.0374	1.08e-06	0.481	0.374	0.0119	0.190	0.0441	0.103
0.653	0.0223	3.08e-06	0.432	0.425	0.0241	0.152	0.0451	0.103
0.653	0.00821	1.16e-05	0.385	0.536	0.0352	0.0844	0.0359	0.120
0.641	0.00436	1.60e-06	0.371	0.497	0.0364	0.159	0.0367	0.128
0.624	0.00164	3.89e-06	0.330	0.633	0.0520	0.104	0.0371	0.139
0.624	0.00770	1.99e-06	0.382	0.503	0.0321	0.153	0.0451	0.169
0.617	0.0268	9.00e-07	0.449	0.404	0.0205	0.198	0.0461	0.192
0.603	0.0334	9.50e-07	0.461	0.376	0.0117	0.189	0.0517	0.0971
0.603	0.0112	2.77e-06	0.509	0.429	0.0149	0.142	0.0645	0.228
0.590	0.0256	1.41e-06	0.566	0.387	0.0117	0.175	0.0531	0.223
0.552	0.0139	3.61e-06	0.466	0.485	0.0268	0.150	0.0382	0.231
0.503	0.0126	1.01e-06	0.434	0.436	0.0285	0.227	0.0335	0.148
0.490	0.0166	2.29e-06	0.438	0.476	0.0350	0.201	0.0286	0.218
0.474	0.0421	7.96e-07	0.482	0.406	0.0276	0.271	0.0292	0.151
0.456	0.0457	4.06e-07	0.417	0.392	0.0322	0.313	0.0284	0.208
0.445	0.0418	5.90e-07	0.416	0.414	0.0341	0.299	0.0263	0.246
0.433	0.0673	3.73e-07	0.561	0.382	0.0226	0.342	0.0246	0.236
0.396	0.000466	1.87e-06	0.422	0.600	0.0637	0.207	0.0163	0.350
0.396	0.000112	1.31e-06	0.315	0.683	0.0980	0.243	0.0143	0.208
0.364	0.00361	1.12e-06	0.487	0.458	0.0292	0.294	0.0137	0.353
0.339	0.00373	1.18e-06	0.483	0.474	0.0330	0.315	0.0116	0.366
0.324	0.00485	1.37e-06	0.506	0.481	0.0338	0.315	0.0106	0.423
0.308	0.00503	1.29e-06	0.493	0.495	0.0377	0.333	0.00963	0.416
0.298	0.00691	8.60e-07	0.521	0.461	0.0340	0.372	0.00957	0.389
0.285	0.00390	7.86e-07	0.486	0.495	0.0370	0.396	0.00858	0.406
0.277	0.000636	1.79e-06	0.429	0.683	0.0796	0.305	0.00688	0.419
0.269	0.000855	1.58e-06	0.411	0.659	0.0784	0.343	0.00578	0.341
0.264	0.000498	2.69e-06	0.425	0.788	0.100	0.307	0.00429	0.356
0.259	0.000267	2.55e-06	0.409	0.841	0.119	0.304	0.00403	0.403
0.255	0.000330	2.82e-06	0.421	0.846	0.113	0.312	0.00375	0.442
0.251	0.000191	2.32e-06	0.391	0.835	0.120	0.331	0.00376	0.447
0.248	0.000578	1.91e-06	0.424	0.764	0.0880	0.412	0.00367	0.477
0.243	0.000293	2.03e-06	0.411	0.843	0.108	0.384	0.00353	0.499
0.240	0.000300	1.93e-06	0.411	0.827	0.105	0.411	0.00325	0.624
0.238	0.000110	1.76e-06	0.347	0.774	0.151	0.265	0.00485	0.270
0.238	0.00150	1.58e-06	0.476	0.697	0.0594	0.482	0.00334	0.572

Figures

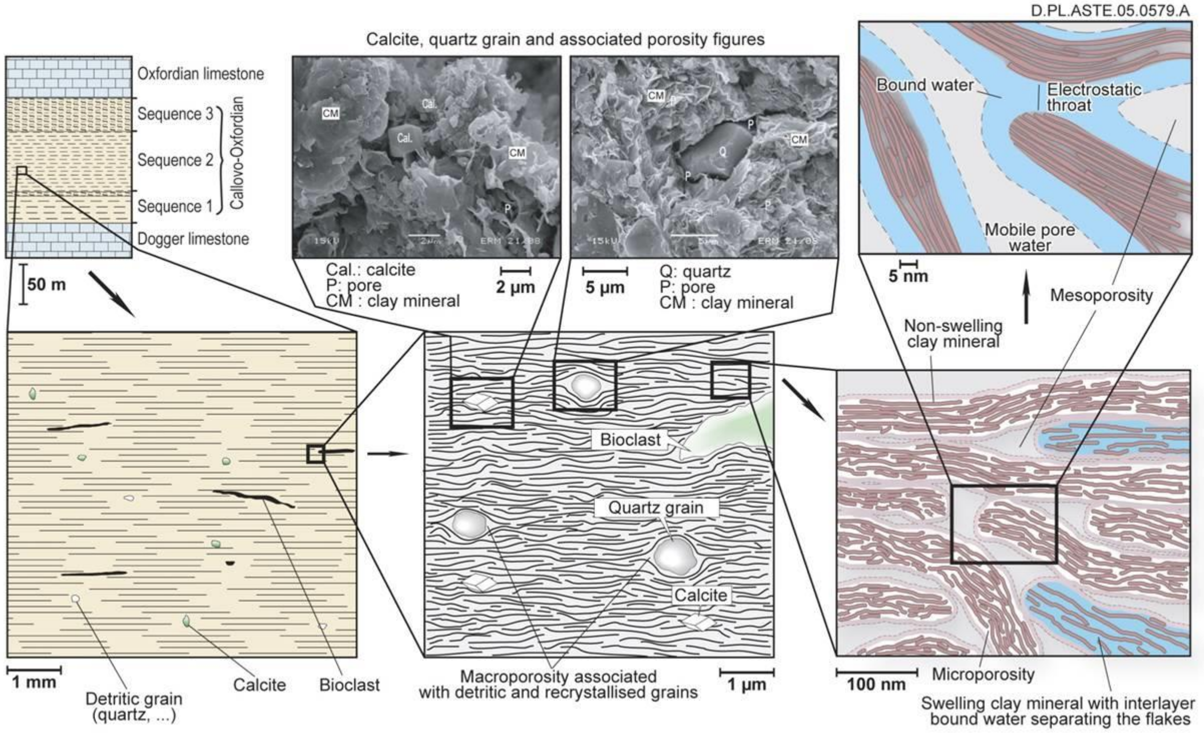

Figure 1. Microstructure of the Callovo-Oxfordian formation illustrating the anistropy of this formation in association with a bedding plane (adapted from Yven et al., 2007). Note however that the anistropy of the Cox formation remains weak (<3 for the permeability).

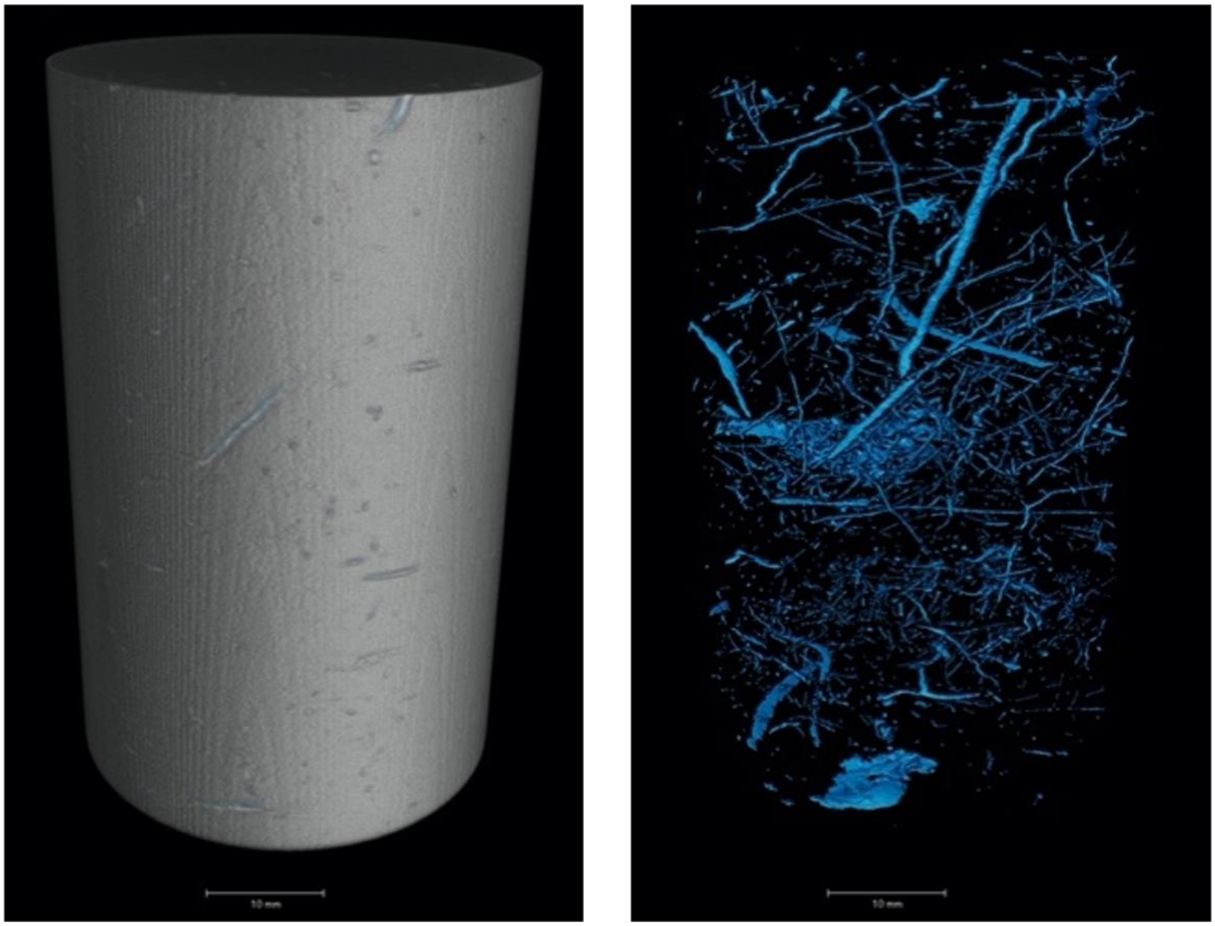

Figure 2. X-ray tomography images of COx sample 59674-41 (cylinder axis perpendicular to the bedding plane) showing the whole volume (left) and the volume of inclusions (pyrite-filled bioturbations) which represents 0.29% of the total volume (right).

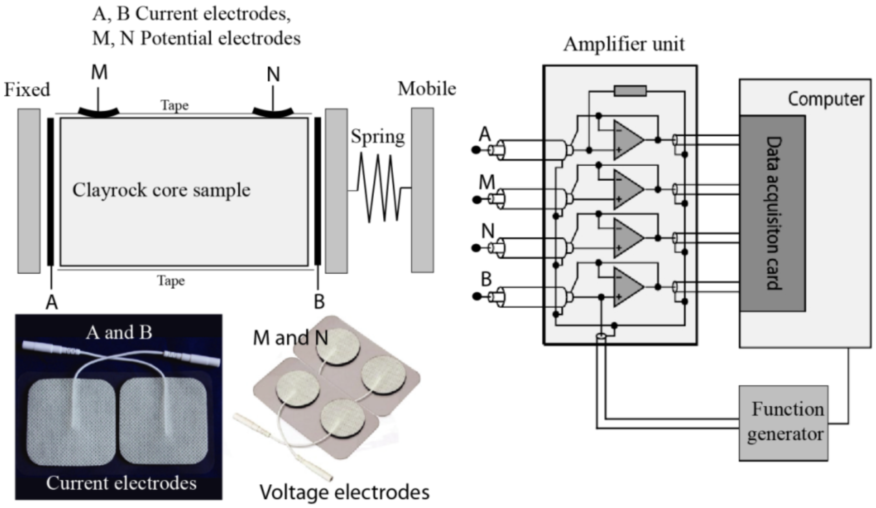

a. Complex conductivity cell

b. ZEL-SIP04-V02

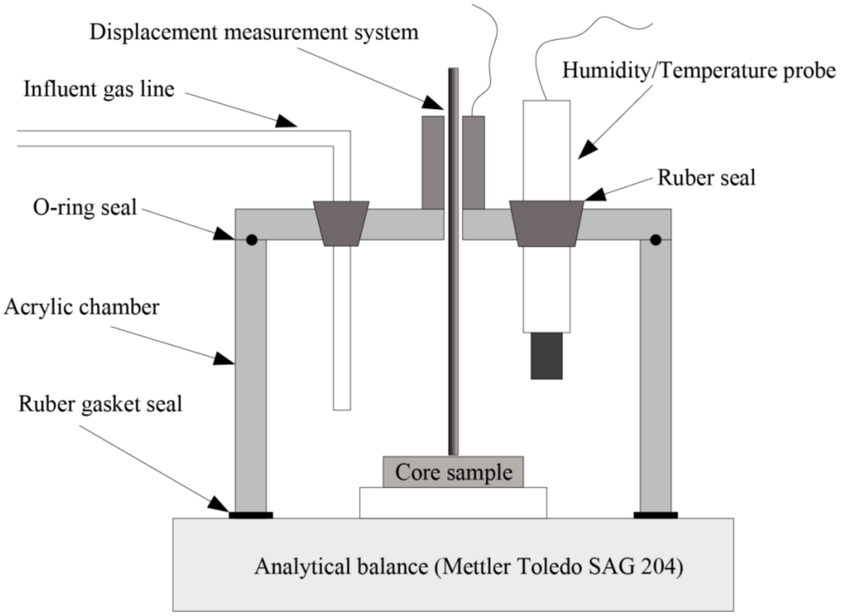

c. Humidity chamber

Figure 3. Equipment used to measure induced polarization for the Collavo-Oxfordian clayrocks. **a.** Sketch of the experimental setup. We used the carbon film electrodes-with hydrogel for injection (A and B) and non-polarizable Ag-AgCl electrodes for potential measurements (M and N). **b.** ZEL-SIP04-V02 impedance meter developed by Zimmermann et al. (2008). This equipment is operated in the frequency range from 1 mHz- to 45 kHz. **c.** Automated humidity system of the environmental chamber in which the measurements are performed (modified from Likos and Lu, 2003).

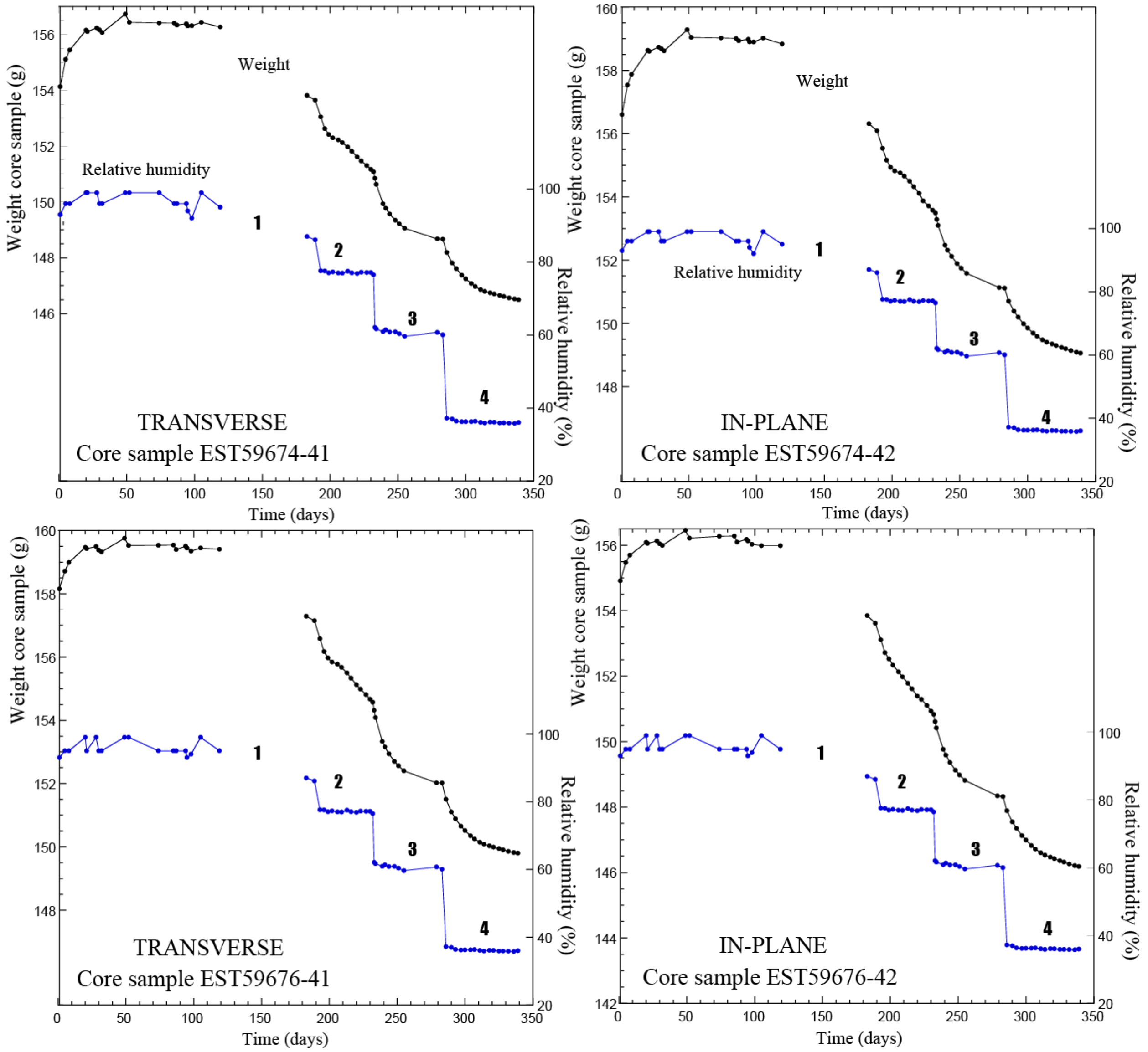

Figure 4. Evolution of the weight of the samples (Cores EST59674 and EST59676) for different relative humidities in a controlled humidity chamber. The saturation steps 3 and 4 is used to characterize the degree of anisotropy of the relative permeability curve of the COx.

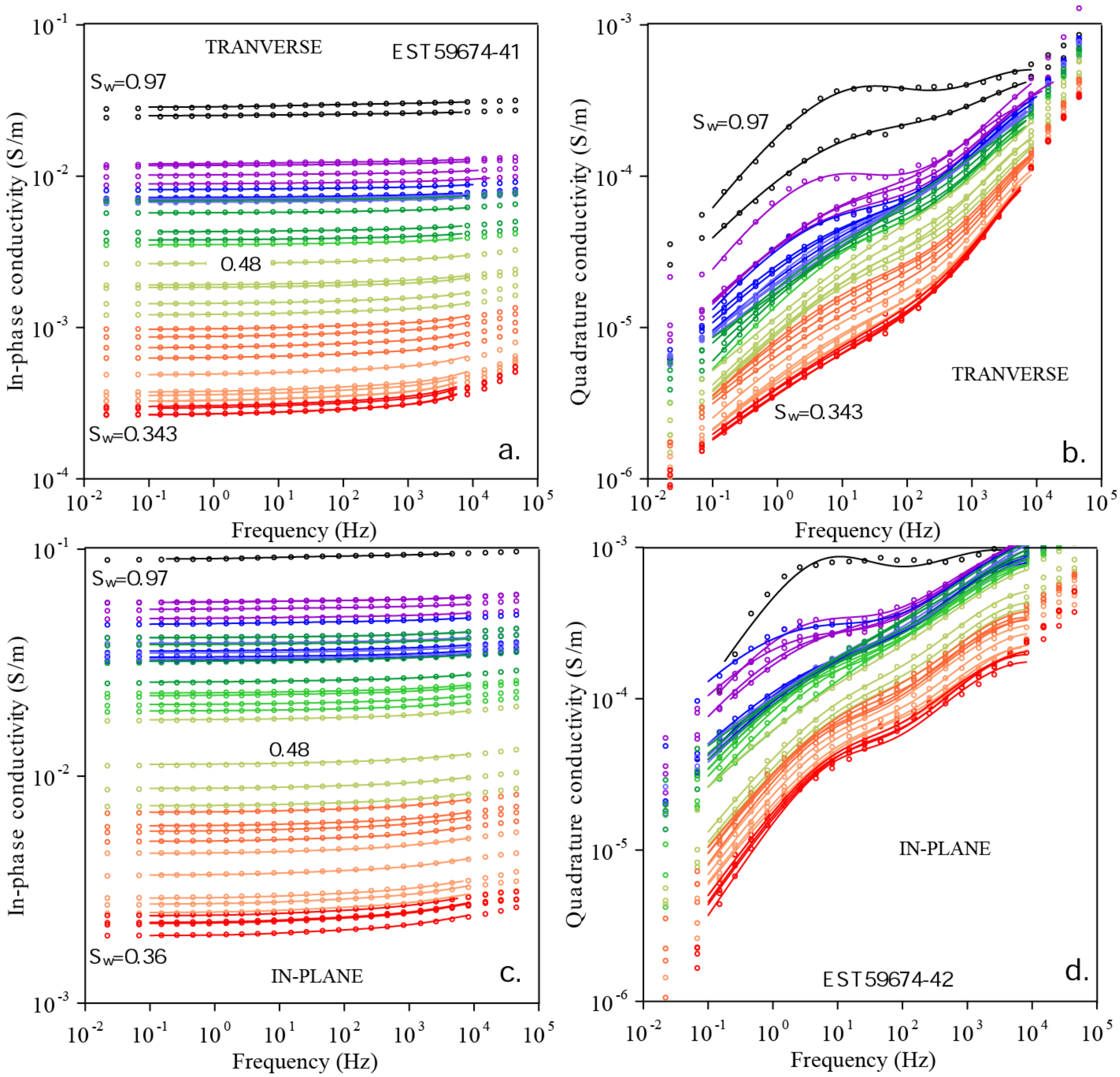

Figure 5. In-phase conductivity and quadrature conductivity spectra for core sample EST59674. **a.** In-phase conductivity, transverse component. **b.** Quadrature conductivity, transverse component. **c.** In-phase conductivity, in-plane component. **d.** Quadrature conductivity, in-plane component. The dots correspond to the measured data while the lines are the fit with a Cole Cole model using a Bayesian approach to optimize the values of the Cole Cole parameters.

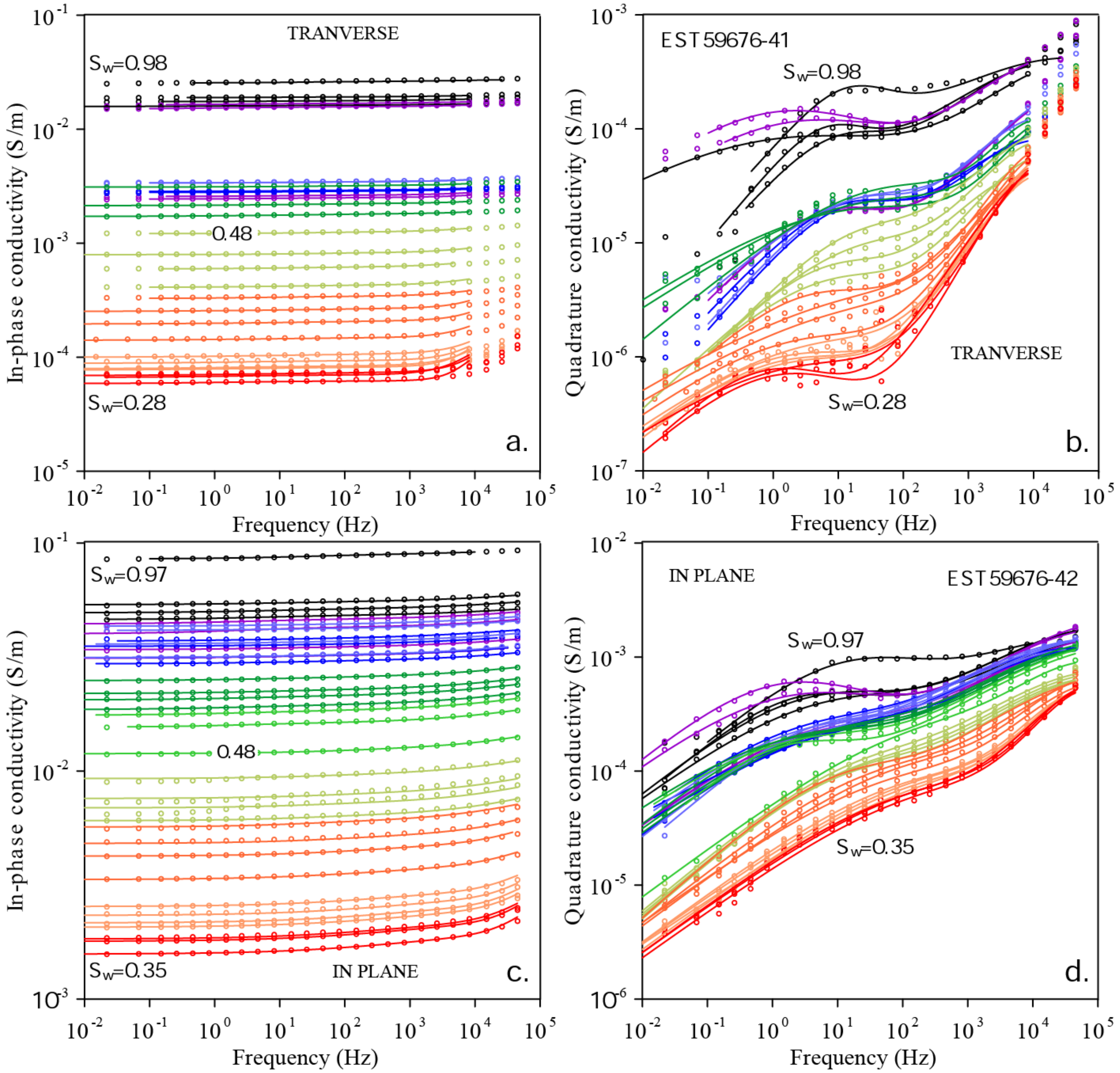

Figure 6. In-phase conductivity and quadrature conductivity spectra for core sample EST59676. **a.** In-phase conductivity, transverse component. **b.** Quadrature conductivity, transverse component. **c.** In-phase conductivity, in-plane component. **d.** Quadrature conductivity, in-plane component.

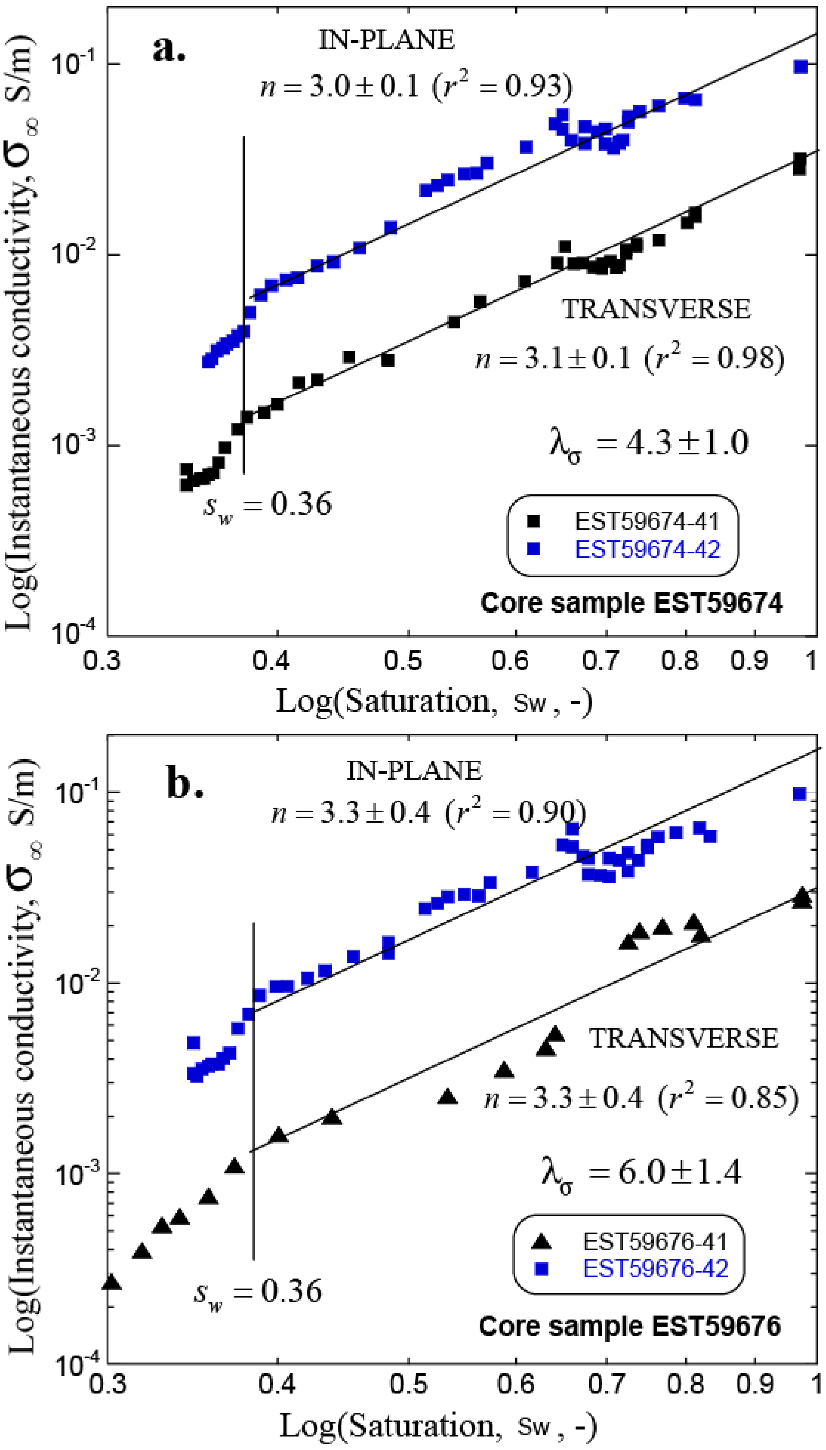

Figure 7. Transverse and in-plane instantaneous conductivity versus pore water saturation in a desiccation experiment. **a.** Core sample EST59674. **b.** Core sample EST59676. Note that the anisotropy ratio is higher for the second core sample. The saturation 0.36 appears as the critical residual saturation, which appears to be independent of the direction of the core smaple.

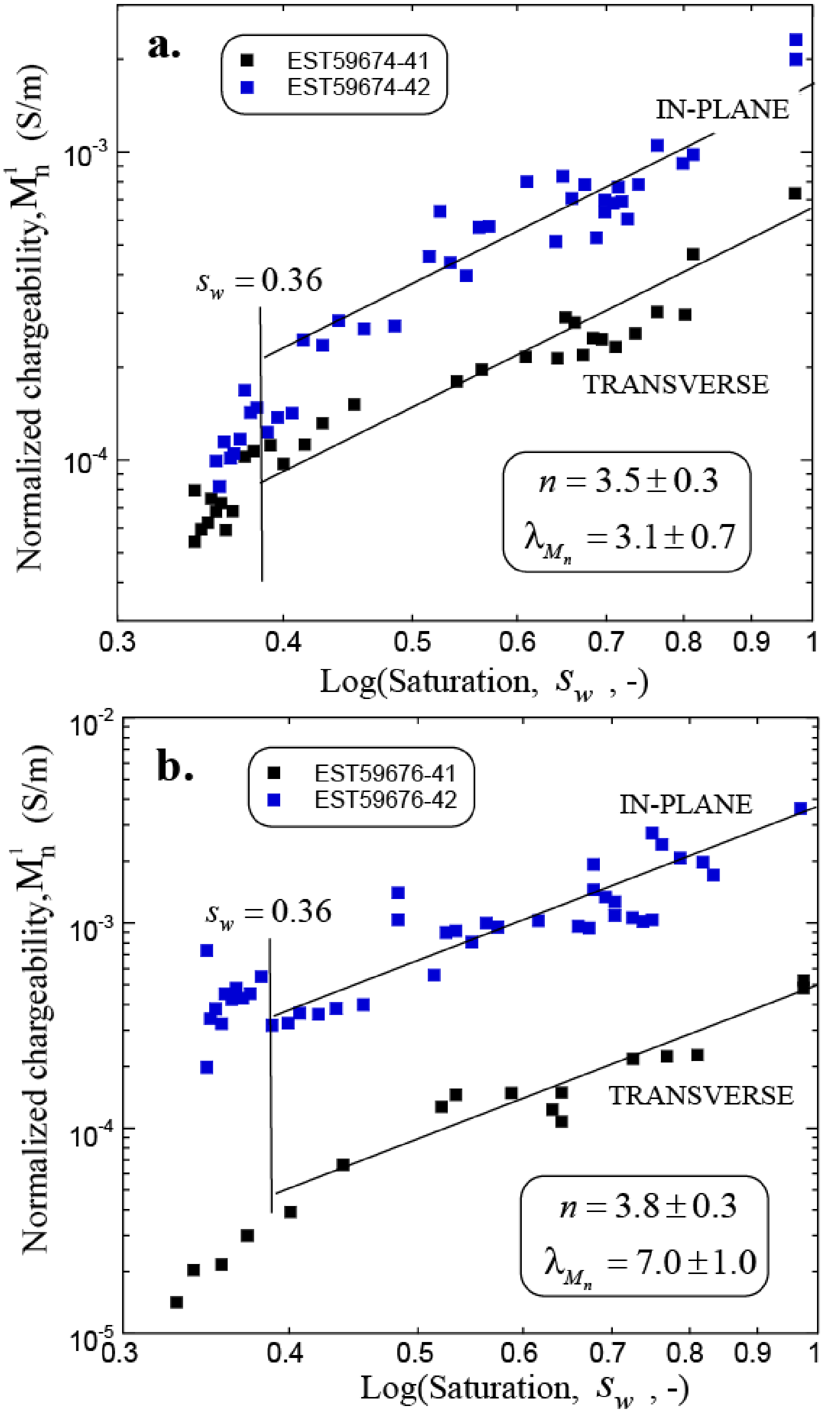

Figure 8. Transverse and in-plane low frequency normalized chargeability versus pore water saturation in a desiccation experiment. **a.** Core sample EST59674. **b.** Core sample EST59676. Note that the anisotropy ratio is higher for the second core sample. The saturation 0.36 appears as the critical residual saturation, which appears to be independent of the direction of the core smaple.

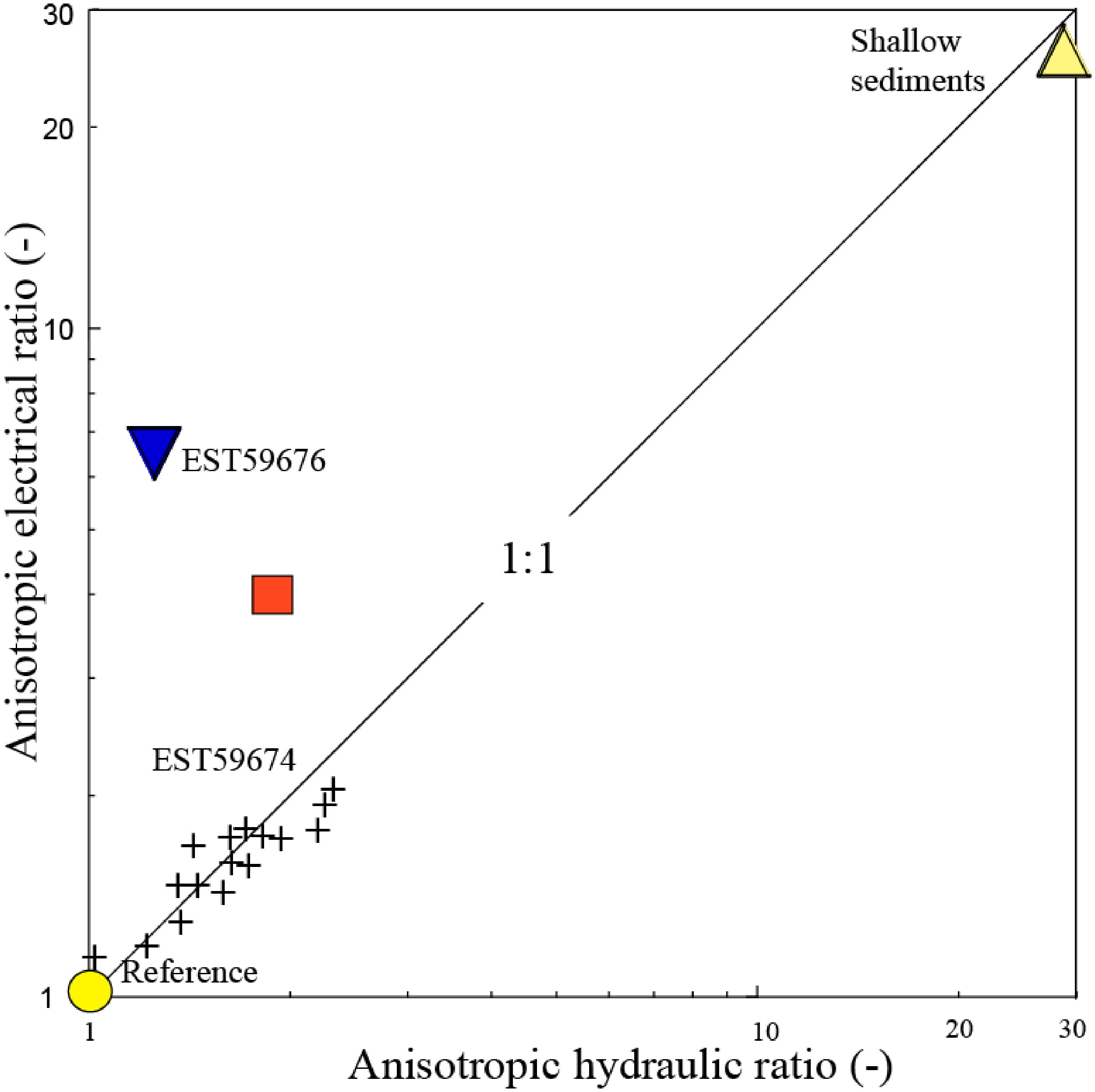

Figure 9. Relationship between the electrical and hydraulic anistropic ratio. This trend should be confirmed with further analysis and data. The data corresponding to shallow sediments (yellow-filled triangle) is from the work of Gernez et al. (2019) based on hydraulic and electrical conductivity tomography. The crosses correspond to mudrocks (data from Adams et al., 2016).

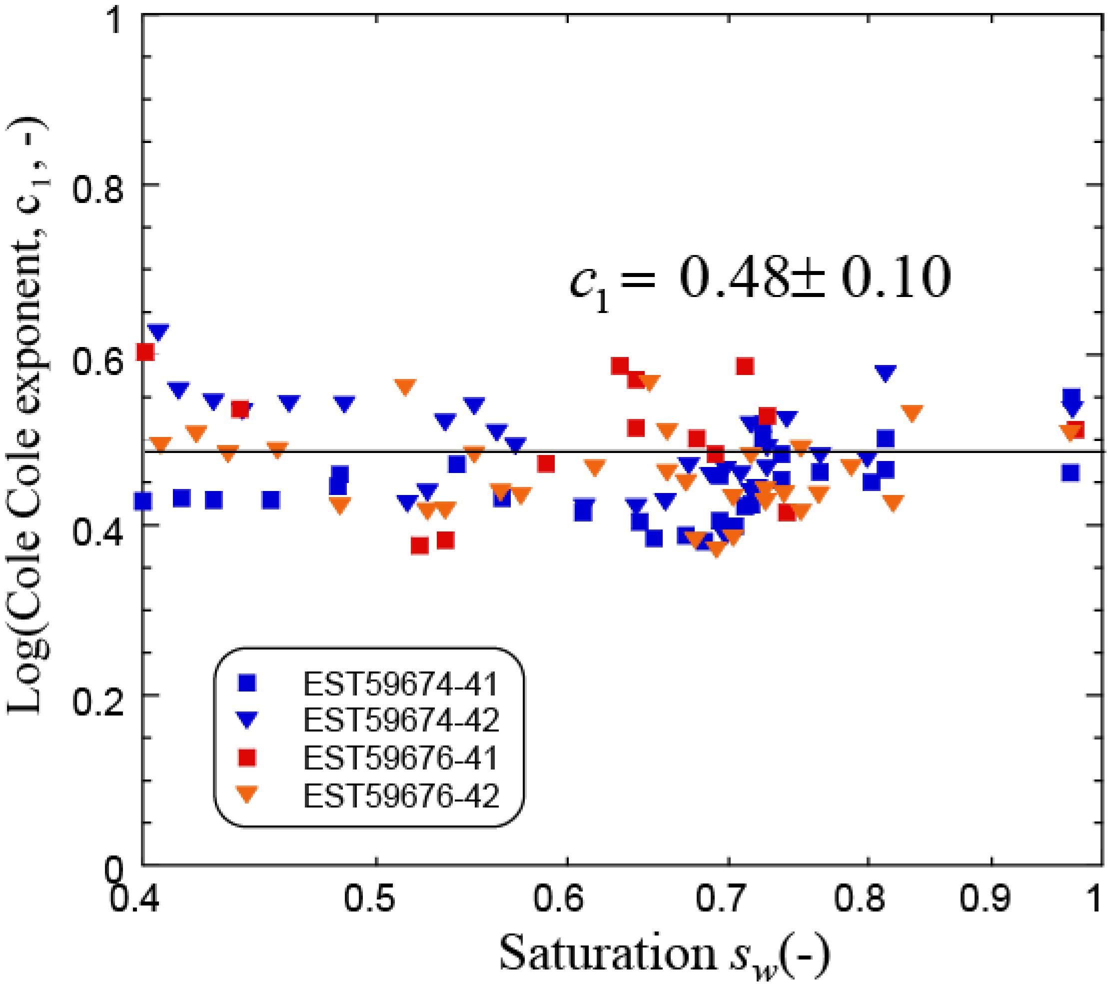

Figure 10. Transverse and in-plane low frequency Cole Cole exponent versus pore water saturation in a desiccation experiment. We use the data of the core sample EST59674 and EST59676.

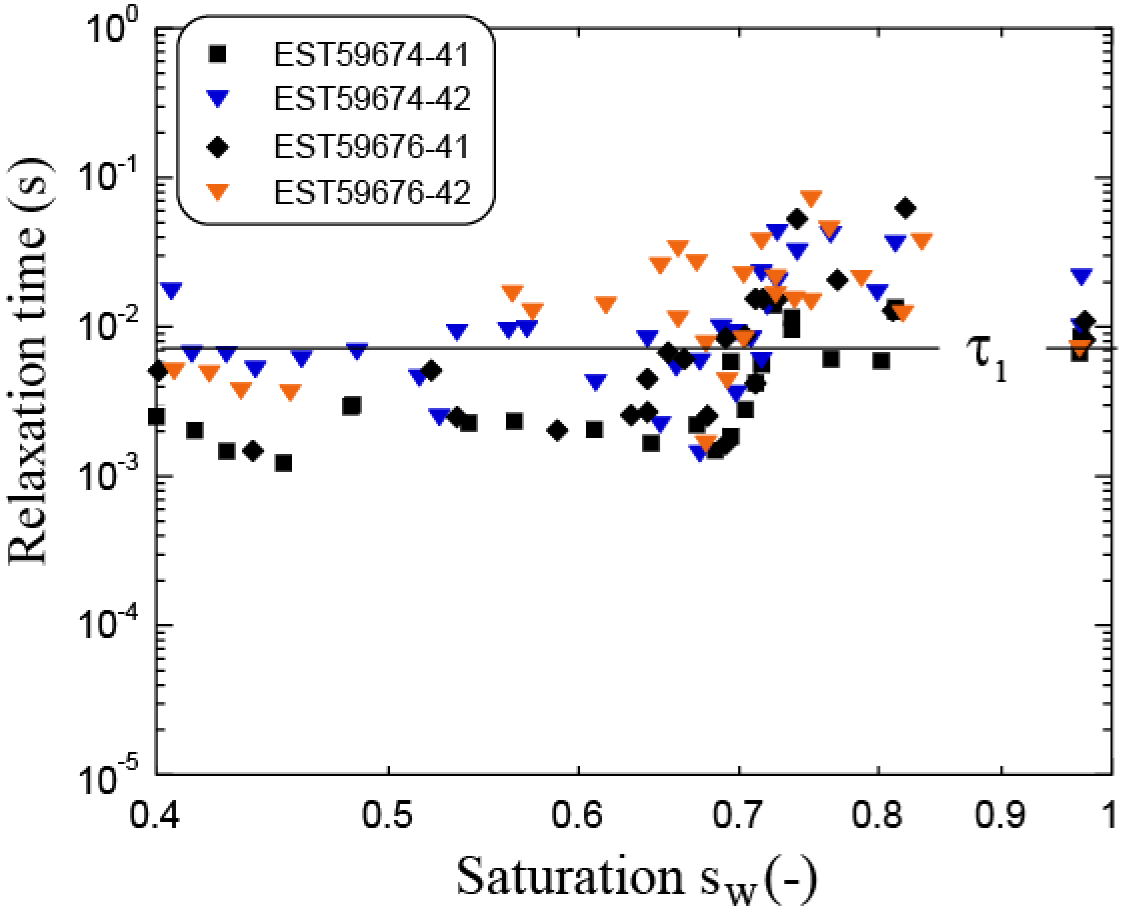

Figure 11. Low-frequency relaxation time versus saturation. The mean value of the relaxation time τ_1 is close to 7×10^{-3} s independent of the direction.

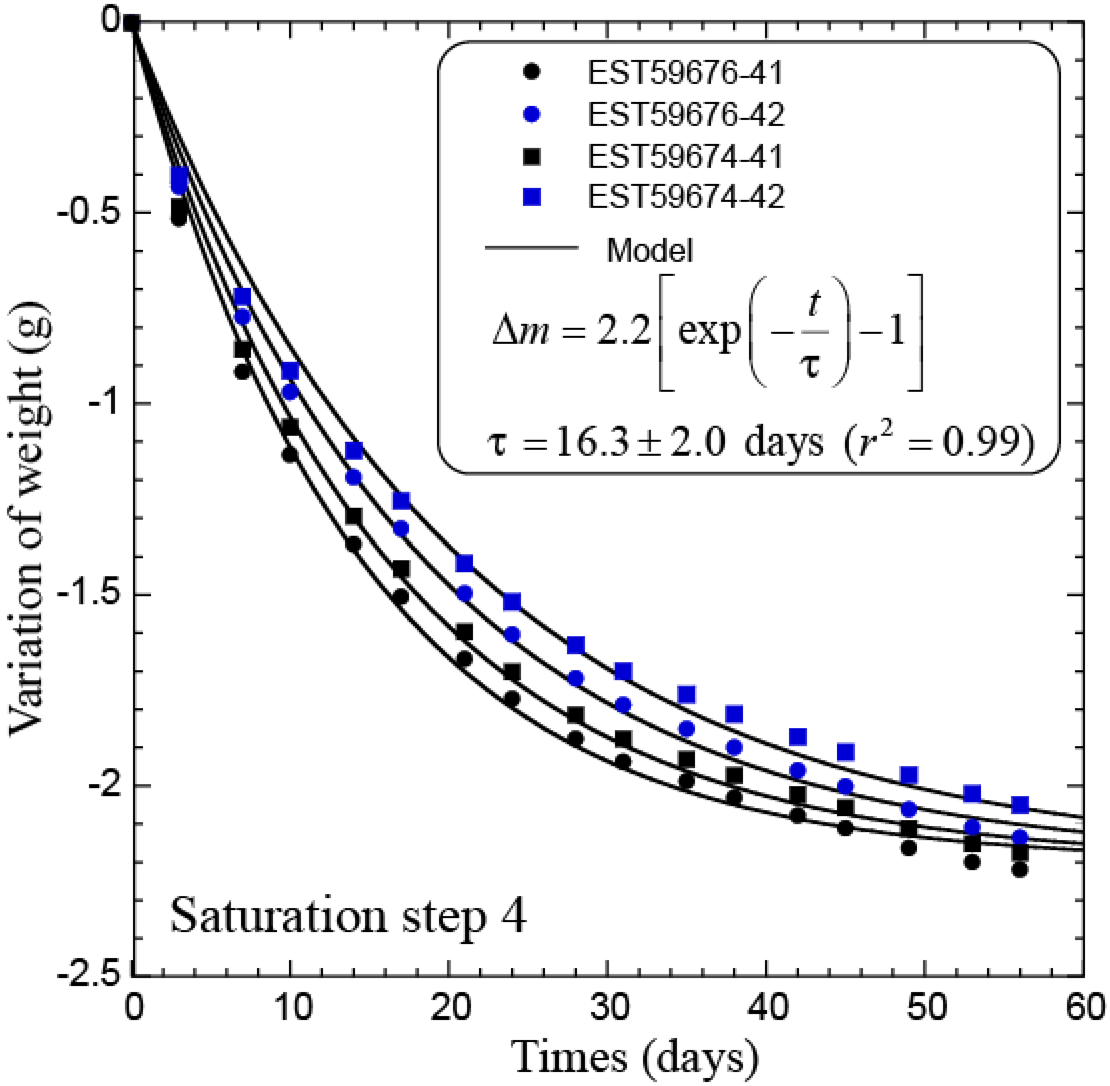

Figure 12. Variation of the weight (in g) of the four core samples as a function of time when the relative humidity in the chamber is changed from 60 to 36% (Step 4 in the data shown in Figure 2). The inverted relaxation times are: (Sample EST59676-1, 14.4±0.5 days), (Sample EST59676-2, 17.7±0.6 days), (Sample EST59674-1, 15.4±0.5 days), and (Sample EST59674-2, 18.3±0.6 days). The data show a small anisotropic effect for the two cores but this effect can be safely neglected.

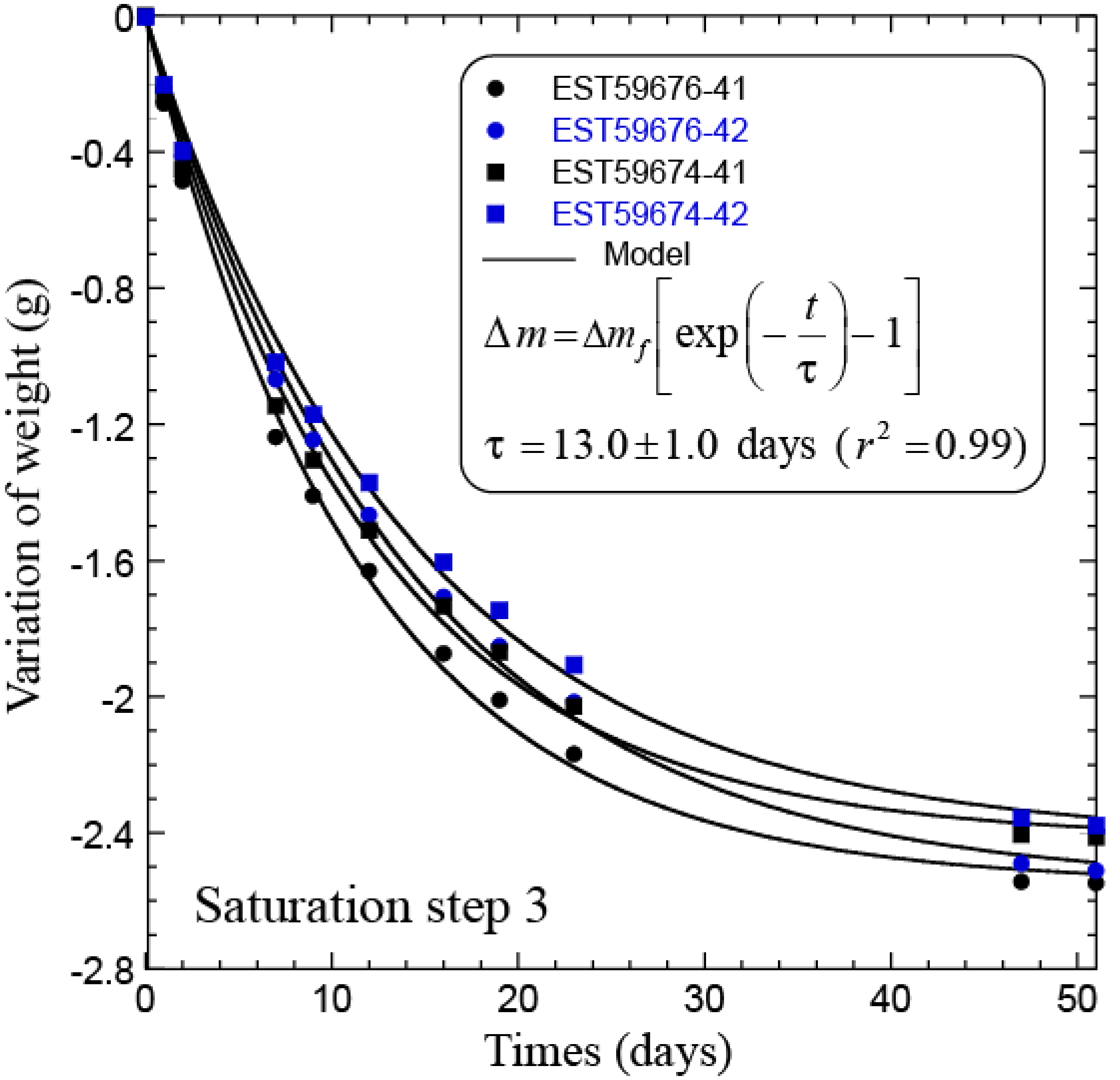

Figure 13. Variation of the weight (in g) of the four core samples as a function of time when the relative humidity in the humidity chamber is changed from 77 to 60% relative humidities (Step 3 in the data shown in Figure 2). The inverted relaxation times are: (Sample EST59676-1, 11.5±0.5 days, Δm_f = 2.6 g), (Sample EST59676-2, 14.0±0.5, days, Δm_f = 2.6 g), (Sample EST59674-1, 12.0±0.5 days, Δm_f = 2.4 g), and (Sample EST59674-2, 14.1±0.6 days, Δm_f = 2.4 g). The data show a small anisotropic effect for the two cores but this effect can be safely neglected.

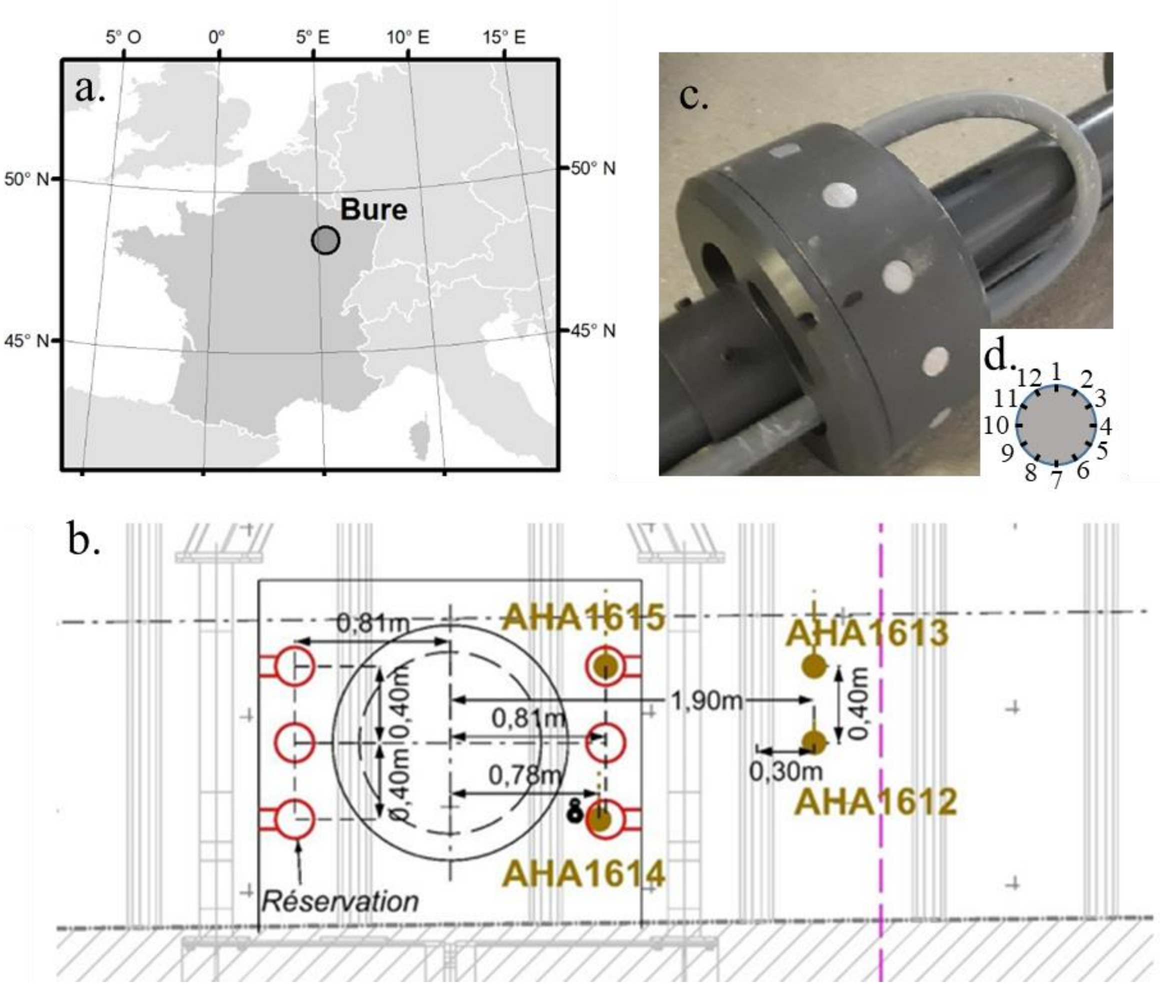

Figure 14. Location of Andra facility at Bure (France) **a.** Borehole location **b.** and Azymuthal electrode system with stainless steel electrodes. This network is used to determine the anistropy of the electrical conductivity and normalized chargeability of the COx formation in *in situ* conditions. **c.** Azymuthal electrode array. **d.** Position of the 12 electrodes used for the study of the anistropy.

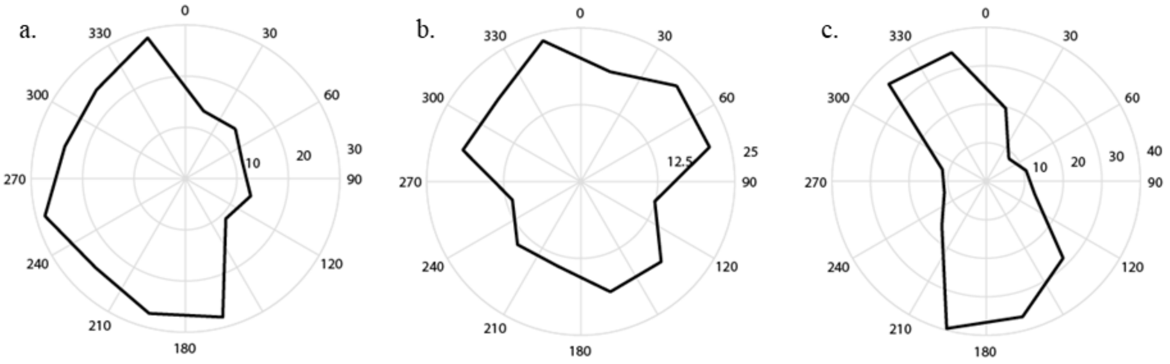

Anisotropy of the electrical resistivity (Ohm.m)

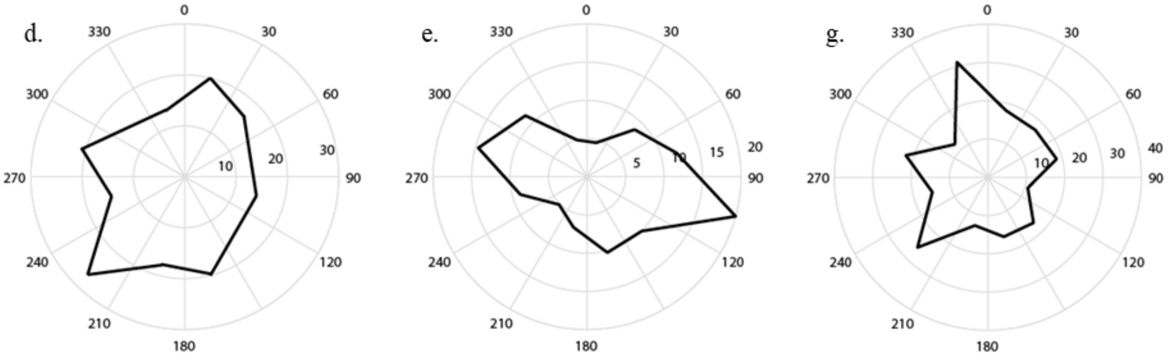

Anisotropy of the chargeability (mV/V)

Figure 15. a. b. c. In situ electrical resistivity based on the azymuthal dipole dipole measurements respectively for the ring 1, 4, 5. The averaged anistropy ratio is 2.3±0.7, which is on the same order of magnitude of the anistropy ratio discussed for the core samples. **d. e. f.,** In situ chargeability (expressed in mV/V) based on the azymuthal dipole dipole measurements respectively for the ring 1, 4, 5. The chargeability does not exhibit a clear anistropy ratio.

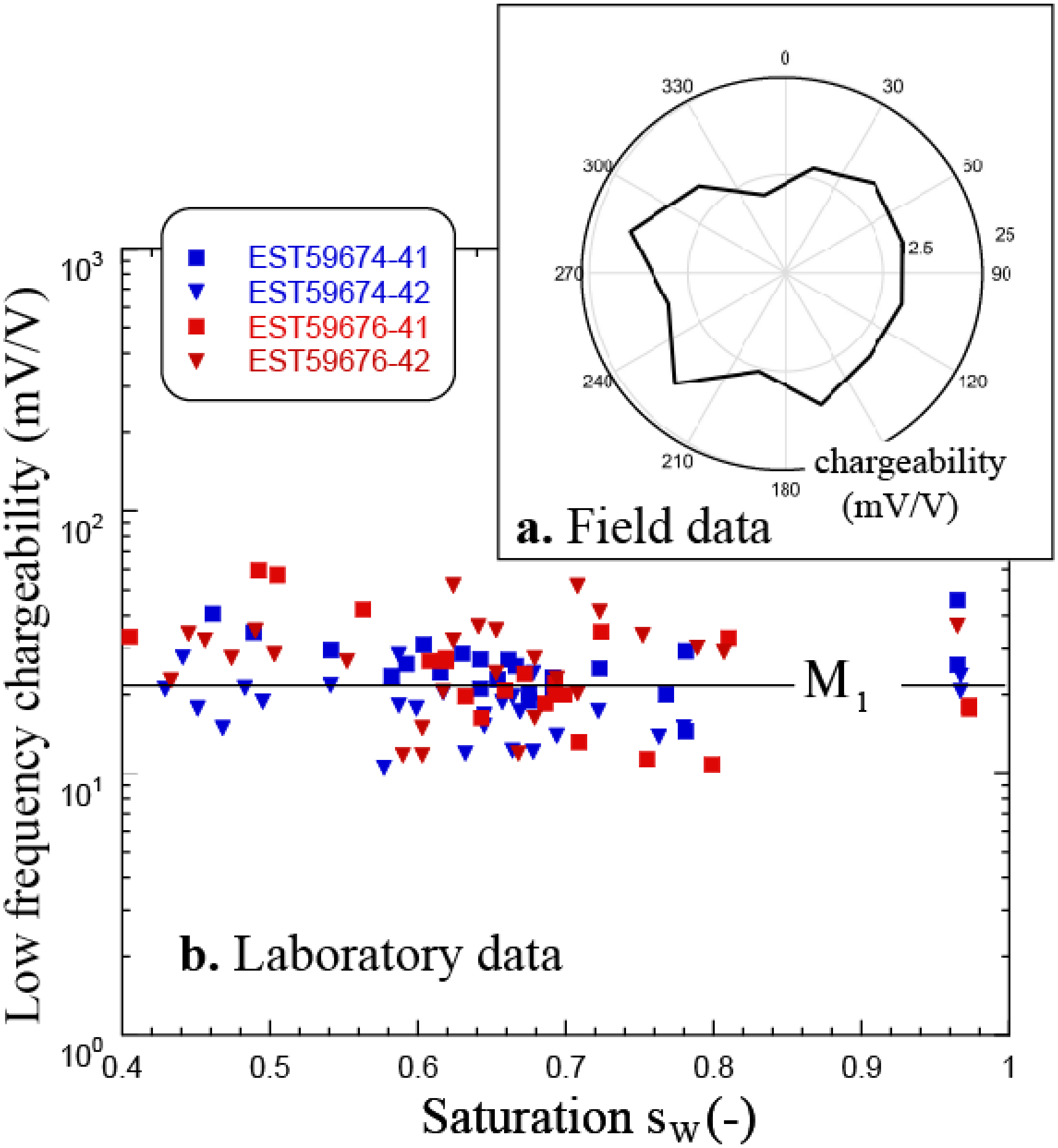

Figure 16. Anistropy of the chargeability. **a.** Field data showing no anistropy of the chargeability of the COx. **b.** Chargeability versus saturation for the four samples used in this study. The data show no anistropy of the chargeability field.